Exploration of Materials and Mesostructures Accessible via Inorganic Phototropic Growth

Thesis by

Kathryn Hamann

In Partial Fulfillment of the Requirements for
the Degree of
Doctor of Philosophy

Caltech

CALIFORNIA INSTITUTE OF TECHNOLOGY
Pasadena, California

2022

(Defended December 8, 2021)

Kathryn R. Hamann
ORCID: 0000-0003-1163-7173

ACKNOWLEDGEMENTS

It’s nearly impossible to recall what I have spent each hour of each day doing over the past few years, but I will always remember the people that were beside during this time. Without them, I’m unsure I’d be here, nearing the completion of my PhD. It’s difficult to fully express the gratitude I feel towards the many people who have supported me over the course of graduate school, but I’ve tried to put it into words here.

First and foremost, I would like to thank my advisor Dr. Nathan Lewis, for giving me a space to learn and grow and for fostering a supportive, compassionate, and enjoyable group culture. Nate is a magnificent scientist and skilled storyteller that is unafraid of tackling big problems and I’m thankful that I’ve had the opportunity to learn from him. I’ve also appreciated Nate’s young spirit and the fun ways he thinks about science. Without a doubt, I will never again see a minion and not think of Nate Lewis. Thanks for everything, Nate.

Thank you to the members of my committee, Geoff Blake, Julia Greer, and my committee chair Harry Gray, for the insight and feedback they’ve given on my work and the time they’ve offered in their busy schedules. I’m honored to have had each of you on my committee.

Thank you to those that have helped keep the Lewis group running throughout the years. Barbara Miralles, we all owe you a tremendous amount of gratitude for all you have done and continue to do for our group. Thank you for keeping our group running seamlessly and for being such a constant source of friendless. Bruce Brunschwig, thank you for all the time and energy you’ve dedicated to keeping instruments in the MMRC running smoothly, and for spending even more time and energy putting up with our group. Bruce’s input is a valuable resource that our group is fortunate to benefit from. Thanks to Kimberly

Papadantonakis for the contributions she's made to our group over the years; Kim's willingness and stubbornness in asking difficult questions is something I'll always admire.

I wasn't exactly sure what I was looking for in a research group when I started graduate school, but I found it exactly in the Lewis group. The Lewis group is a delightful collection of people that do incredible science but also embrace silliness and never take themselves too seriously. I'd like to thank all of the Lewis group members with whom I overlapped during my time, no matter how brief it was: Noah Plymale, Nick Batara, Fadl Saadi, Josh Wiensch, Jingjing Jiang, Xinghao Zhou, Dan Torelli, Michael Lichterman, Jonathan Thompson, Azhar Carim, Stefan Omelchenko, Sisir Yalamanchili, Annelise Thompson, Paul Nuñez, Ivan-Moreno Hernandez, Ellen Yan, Ethan Simonoff, Paul Kempler, Kat Rinaldi, Kyra Lee, Pai Buabthong, Katie Chen, Weilai Yu, Kathleen Kennedy, Harold Fu, Michael Mazza, Madeline Meier, Zach Ifkovits, Mo Morla, Jackie Dowling, Sean Byrne, Jake Evans, Alex Ye, Ke Sun, Matthias Ricther, Carlos Read, Miguel Cabán-Acevedo, Burt Simpson, and Renata Balgley. Thank you all for making the Lewis group a great spot to work and learn.

As a result of the Lewis group being comprised of such wonderful people, several of my coworkers have become close friends. I'd like to thank the following group members explicitly, you each have made my time at Caltech distinctly great. Azhar Carim has helped me tremendously both inside the lab and out, as both a scientific mentor and a friend. I am incredibly thankful for all of the guidance he has provided in my work and for the contributions he has made to our group as a whole. Azhar is an incredibly talented and hardworking scientist who never lets an occasion go uncelebrated, and that is something I've grown to appreciate. Thank you for working alongside me throughout the years, especially during the long hours spent in lab during the "Winter of Squiz," and for the helpful comments in the preparation of this thesis and other written works and presentations. Beyond the lab, thank you for acting (usually simultaneously) as an event planner, Lewis group historian, bartender, chauffeur, crawfish deliveryman, and everything in between. Thanks for pushing me to become a better scientist, for teaching me that there is no job too big, small, or mismatched for a Dremel, and for literally always being down for a pretzel and a beer. I first met Jackie Dowling not through the Lewis group, but as a randomly assigned roommate my second year (although her first words to me were, "So you're in the Lewis group?!"). She ended up joining me in the Lewis group and since then it's hard to imagine my graduate school path without her—she has simultaneously been my labmate, officemate, and roommate for the majority of my time at Caltech. Jackie continually inspires me to be intellectually curious and has provided indispensable support and companionship during graduate school and beyond; I am so grateful for whatever lottery system paired us as roommates. Thank you for being the most incredible hype man and an even better friend, for supporting me during the lows and celebrating me during the highs, and for bringing unmatched energy and eagerness to every occasion. Thanks for always making our little house so loving and lively (especially during quarantine) and for dragging me on so many great adventures, be it on skis or on scooter; I'll always treasure the memories and enumerable laughs and I look forward to many more. I'm thankful to have had Madeline Meier join the Squiggles subgroup, she has been essential in much of the simulation work presented throughout this thesis. Thanks for all the collaboration, for being a great leader and presence within the group, and for usually siding with me whenever Azhar came up with crazy ideas. Outside of the lab, thanks for being a fellow coffee and pasta lover, I've appreciated all the coffee trips we've made and all the delicious recipes we've shared. Sisir

Yalamanchili, thanks for being the group's best puma hunter and for always being willing to jump in on any adventure, whether it was exploring a cool new hike or finding the best boba or dumpling spot in the greater LA area. Thanks for going along with the shenanigans of Madeline, Azhar, and I, and keeping us all entertained with your Sisir-isms.

I owe so much gratitude to the Squiggles subgroup for being the best collection of people to work with within the Lewis group. Jonathan Thompson and Ethan Simonoff, thanks for being great resources on anything squiggles (and beyond) and for being a constant source of entertainment—your unending antics always kept me giggling. I'd also like to thank Jonathan for his knowledge on 21-Ohm resistors. I'm grateful to have shared so much collaboration with Azhar Carim and Madeline Meier; thanks for being great teammates and even better suppliers of Lab Snacks. Sean Byrne, thanks for joining me in the "non-SeTe" sector of the Squiggles subgroup, always having a positive and upbeat presence, and being a worthy Bananagrams opponent.

I'd like to thank my classmates within Lewis group: Michael Mazza, Harold Fu, Weilai Yu, Kathleen Kennedy, and Katie Chen. Thank you for the support in navigating our first year in the group. I'd especially like to thank Michael Mazza for his willingness to take on various roles within the group, whether it be Noyes safety officer or Cold Fusion team captain. As the last to graduate of this class, it has been a pleasure getting to watch each of you grow as a scientist and advance onto new and bigger things.

I've hopped around offices during my time but was always surrounded by great people. To the inhabitants of Jorgensen G131, Ke Sun, Jingjing Jiang, Sisir Yalamanchili, Weilai Yu, Kimberly Papadantanakis, Eric Verlage, Jinghao Xao, Stefan Olmanchenko, Paul Nunez, Kathleen Kennedy, and Katie Chen, thank you for welcoming me into the office and for the insightful discussions along the way. To the recent inhabitants of Jorgensen G135, Jackie Dowling, Zach Ifkovits, and Madeline Meier, thanks for reviving the office after a long hiatus and making it an enjoyable (even if occasionally distracting) place to work, and for teaching me how to solve more types of Rubik's cubes than I even know existed, although I think I've already forgotten how to by now.

Thank you to Nathan Zou, who joined me in the lab as a SURF student, for being willing to jump in on several projects throughout the past summer and for being an enjoyable labmate to work with. I'd also like to thank the other Lewis group SURF students of this cohort: Maddie Swint, Anna Li, and Sarah Kabboul. Thanks to all of you for joining in on Lewis group shenanigans and for bringing some youthful life into the office.

I'd also like to acknowledge some of the additional resources that were instrumental in preparing me for and supporting me throughout my PhD. Thank you to the faculty and my classmates in the chemistry departments at both New Mexico Highlands University and Eastern Oregon University for giving me the knowledge, curiosity, and confidence to pursue a PhD in chemistry. My PhD work was partially funded by the "Light-Matter Interactions" Energy Frontier Research Center, I am grateful for all of the scientific discussions (and pizza) that came from this collaboration—thanks to those involved for your contributions. Alison Ross in the CCE graduate office was consistently a helpful and friendly resource in navigating degree progress requirements or any other questions that arose. Nathan Hart in the Caltech glass shop was instrumental in building photoelectrochemical cells used for nearly every experiment conducted in this thesis, and I always appreciated the speed and creativity with which he was able to fabricate whatever crazy new cell design we came up with. I'm particularly grateful for two Lewis group alumni, Dan Torelli and Nick Batara, for

the insightful discussions and advice they have given on career paths post-PhD. I'd also like to give a special shout-out to the women of the Lewis group, thank you for the support and coffee trips throughout my time here, you are all awesome and inspiring women in STEM and I've appreciated each of you in navigating this career path.

Last, but certainly not least, I owe a tremendous amount of thanks to my friends and family. Thank you to the Gibson family, as well as the broader Gibson Ranch community, for giving me a home away from home during my time in LA. To Ted Rothenberg, thank you for all of the love, support, and positivity you have provided during the final years of my PhD. To my Mom, words aren't enough to express my love, gratitude, and admiration. Thank you for everything: for the love and encouragement you have given me, for teaching me the value of hard work and independence, and for raising me to be the person that I am today. Thank you for giving me the confidence and support to take on new challenges and for being just a phone call away when those challenges get hard. I owe all of my successes to you. Finally, to the friends and family not mentioned here by name, this letter is by no means exhaustive. You all have supported me in so many ways, big and small, and I truly appreciate each and every one of you beyond what I can possibly express here in words.

If you have read this far, thank you for bearing with me! This PhD has been an incredible journey and it wouldn't have been possible without the support of those mentioned here. Thank you all.

Katie Hamann

December 2021

Pasadena, CA

ABSTRACT

Biological systems have evolved complex methods to interact with and adapt to a given environment to optimize fitness, and replication of these natural mechanisms in artificial systems has been a long-standing area of research interest with significant potential utility. Phototropic growth is a natural phenomenon wherein an organism spatially orients biomass addition to optimize light collection. An artificial analog, inorganic phototropic growth, has been demonstrated and relies on a similar process: semiconductor mass is selectively added near regions of high light absorption, thus optimizing light collection and instructing further localized material addition. Inorganic phototropic growth effected via light-mediated electrodeposition has been used to generate anisotropic Se-Te mesostructures with optically-defined morphologies by capitalizing on inherent asymmetries in light absorption at structured, semiconducting interfaces to direct anisotropic growth. This thesis broadens the previous understanding of inorganic phototropic growth via a series of investigations that expand both the material library and complex morphologies accessible and includes detailed analyses of associated structural evolutions and the underlying optical phenomena. First, inorganic phototropic growth of highly ordered and periodic PbSe and CdSe mesostructures with optically-defined morphologies is demonstrated. Second, deposition using temporally varying illumination inputs to generate Se-Te mesostructures with tunable morphological complexity in both the in-plane and out-of-plane directions is examined. Third, the use of single, static, short wavelength (green to ultraviolet) inputs to simultaneously define two orthogonal sets of periodic features in Se-Te deposits is explored. A suite of optically-based simulations is used throughout to model the growth processes and elucidate the fundamental light-matter interactions which defined the empirically observed morphologies.

PUBLISHED CONTENT AND CONTRIBUTIONS

Portions of this thesis have been drawn from the following publications:

Carim, A. I.*; Hamann, K. R.*; Batara, N. A.; Thompson, J. R.; Atwater, H. A.; Lewis, N. S. Template-Free Synthesis of Periodic Three-Dimensional PbSe Nanostructures via Photoelectrodeposition. *J. Am. Chem. Soc.* **2018**, *140*, 6536–6539. DOI: 10.1021/jacs.8b02931.

> K.R.H. performed the experiments, analyzed the data, and helped prepare the manuscript. *(*equal author contributions)*

Hamann, K. R.*; Carim, A. I.*; Meier, M. C.; Thompson, J. R.; Batara, N. A.; Yermolenko, I. S.; Atwater, H. A.; Lewis, N. S. Optically Tunable Mesoscale CdSe Morphologies via Inorganic Phototropic Growth. *J. Mater. Chem. C* **2020**, *8*, 12412–12417. DOI: 10.1039/D0TC02126A.

> K.R.H. performed the experiments, analyzed the data, and helped prepare the manuscript. *(*equal author contributions)*

Hamann, K. R.; Carim, A. I.; Meier, M. C.; Lewis, N. S. Path-Dependent Morphological Evolution of Se–Te Mesostructures Prepared by Inorganic Phototropic Growth. *J. Am. Chem. Soc.* **2020**, *142*, 19840–19843. DOI: 10.1021/jacs.0c09798.

> K.R.H. designed and performed the experiments, analyzed the data, and prepared the manuscript.

Hamann, K. R.; Meier, M. C.; Lewis, N. S.; Carim, A. I. Plastic Morphological Response to Spectral Shifts during Inorganic Phototropic Growth. *JACS Au* **2022**, *2*, 865–874. DOI: 10.1021/jacsau.1c00588.

> K.R.H. designed and performed the experiments, designed and performed the simulations, analyzed the data, and prepared the manuscript.

Hamann, K. R.; Carim, A. I.; Meier, M. C.; Lewis, N. S. Emergent Generation of Mesostructures with Dual, Orthogonal Interfacial Periodicities *via* Inorganic Phototropic Growth. *In Preparation.*

> K.R.H. designed and performed the experiments, analyzed the data, and prepared the manuscript.

TABLE OF CONTENTS

LIST OF FIGURES

Chapter 1

INTRODUCTION AND BACKGROUND

1.1 Background

In nature, living organisms exist not in isolation, but rather as a part of a larger ecosystem and within a surrounding environment. Organisms are thus affected by external forces and stimuli and have evolved to optimize interactions with the surrounding environment to maximize biological fitness. For example, nature spontaneously generates ordered, mesostructured interfaces which exhibit unique and beneficial optical, physical, and mechanical properties.[1–8] Many species of insects have corneas composed of densely packed nanostructures which reduce scattering losses and enhance light sensitivity.[3,9] The vibrant wing coloration of many butterfly and beetle species is a consequence of interfacial nanoarchitectures which act as diffraction gratings and produce strong iridescence.[10–17] Shark skin, lotus leaves, and cacti all have unique mesostructured interfaces which allow for reduced drag, superhydrophobicity, and directional water collection, respectively—each a beneficial trait for the respective surrounding environment in which the organism exists.[18–23]

Biological systems demonstrate phenotypic plasticity whereby an organism expresses different phenotypes in response to changes in the local environment.[24] Plasticity provides for the adaptive exhibition of a diversity of morphologies to maximize fitness in variable environments. Plants exhibit a high degree of phenotypic plasticity to compensate at least partially for their intrinsic inability to avoid unfavorable locations by movement, due to the absence of motility in organisms in this biological kingdom.[25] Moreover, resources that are essential for plant growth are usually distributed heterogeneously within the habitat.[26] Plants thus modulate the construction of resource gathering organs, such as root tips and leaves, and are capable of selective placement of these structures to maximize the potential for resource acquisition.[27] Flood-resistant plant species can form aerated root tissue within days of flooding, enabling gas diffusion and preventing root death; members of the genus *Rumex* increase shoot elongation rates within hours of flooding to reestablish air contact.[28] Plants are predominantly photosynthetic organisms that depend on solar insolation for energy, and thus demonstrate marked phenotypic plasticity to manage this resource.[29] Plants can display a photomorphogenic response to changes in the spectral distribution of the available illumination.[30,31] The process of phototropic growth, in which the addition of biomass is guided in a feedback loop to optimize harvesting of sunlight, allows plants to exhibit spatially directed growth in response to illumination.[32–35] Cucumber plants, which are shade-intolerant, can colonize horizontally patchy environments by preferentially projecting leaf area into light gaps.[36] Numerous trees, including palms and certain species of pines, and flowering plants exhibit inclined growth toward the equator, wherein photosynthetic mass addition occurs in the direction in which the time-averaged solar intensity is maximal, to optimize light collection.[26,29,30]

A significant amount of work has been directed toward the synthesis of biomimetic systems that resemble organisms or structures in nature in form, function, or behavior.[37–47] Recently, an artificial inorganic phototropic growth process was described wherein Se-Te films were generated via a light-mediated electrodeposition technique.[48,49] The synthesis resulted in highly ordered, periodic, and anisotropic mesostructured interfaces which were principally defined by the illumination conditions used during growth.[50–52] Optically-based simulations of the growth process successfully reproduced the experimentally observed morphologies using limited empirical inputs and suggested that the growth process was directed by fundamental interactions between the light and the semiconducting film.[48,53] Inorganic phototropism is thus analogous to natural phototropism in that the addition of absorber mass is localized to areas of high light absorption and the film morphology evolves to optimize light collection. The Se-Te films exhibited a morphological plasticity wherein the exact pattern generated was uniquely defined by the illumination inputs provided. The inorganic phototropic growth process was effected using a scalable and facile solution-based, benchtop technique that did not require elevated temperatures, reduced or elevated pressure, substrate pre-patterning, nor the generation of structured light fields.[48,54,55] Illumination was provided by conformal, incoherent, and low-power light-emitting diode (LED) sources, and ordered mesostructures with nanoscale features were generated over macroscopic, square-centimeter areas in minutes.

1.2 Fundamentals of Photoelectrodeposition

Inorganic phototropic growth has been used to generate mesostructured semiconducting Se-Te films via light-driven electrochemical deposition. A brief background on electrodeposition, photoelectrodeposition and semiconductor materials is provided here; additional resources should be consulted for a more thorough background on the fundamentals of electrochemical processes and semiconductor physics.[56–58]

In electrochemical reactions, chemical, and in some cases physical, change is effected via the transfer of electrons across a heterogenous interface and charge transport through a conductive circuit. Electrochemical processes can be described as either cathodic, wherein an electrode donates an electron to a species that becomes reduced, or anodic, wherein electrons flow into an electrode from a species that becomes oxidized. A complete electrochemical reaction is composed of two paired half-reactions, one anodic and one cathodic, either of which can occur at two spatially separated electrodes, a working electrode and a counter electrode, that are separated by a conductive electrolyte phase. In many cases, only one half-reaction is of interest and discussed, as is the case in the remainder of this section and throughout this thesis. The half-reaction of interest takes place at the working electrode. At all times, a charge-balancing half-reaction must occur simultaneously at the counter electrode at the same rate (current) as the reaction of interest is proceeding at the working electrode. For cathodic processes at a working electrode in aqueous solution, water oxidization is often effected at the counter electrode.[57]

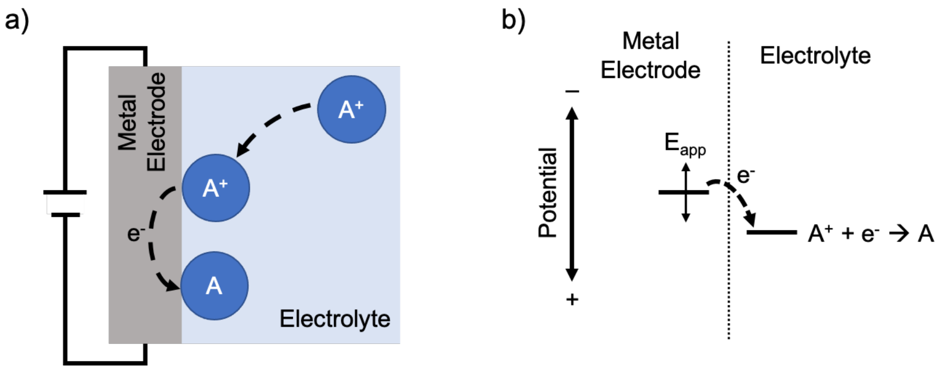

Figure 1.1 (a) Schematic of cathodic electrodeposition. A solution phase species, A^+, accepts an electron at the working electrode interface, is reduced to A, and deposits as a solid phase, on the surface. (b) Energy diagram of the electrodeposition process shown in (a). The reduction potential of species A^+ in solution is intrinsically set. The potential of electrons in a metal electrode can be arbitrarily defined by applying a potential, E_{app}. Raising the potential of the metal electrode above the A^+/A redox potential enables electron transfer across the interface and concomitant material deposition.

Figure 1.1a presents a schematic that illustrates cathodic electrodeposition at a metal electrode surface. An external reductive bias is applied to a working electrode and electrons are transferred across the solid/liquid interface to oxidized species A^+ in solution, which become reduced and form a solid phase A on the electrode surface. Figure 1.1b presents a simple energy diagram for the electrodeposition process shown in Figure 1.1a. The redox potential of the A^+/A couple in solution has an intrinsically defined value. To effect electrodeposition, the potential of electrons at the working electrode must be more negative than the A^+/A reduction potential. The energy of the electrons in the metal can be raised or lowered by applying a potential (E_{app}) with an external energy source, typically accomplished using a potentiostat in the laboratory. Electrodeposition has been widely demonstrated for the synthesis of thin films of metals, oxides, alloys, semiconductors, polymers, and two-dimensional materials.[59–73] Furthermore, the technique is solution-based and is thus scalable, tunable, has high throughput and atomic efficiency, and is low cost relative to commonly used vapor deposition techniques.[74–76]

Electrodeposition on a conformal metal electrode is a spatially homogenous process: the entire surface is at equipotential and charge carriers are available for electrochemical reactions at all spatial locations across the electrode. Lithography can be utilized to pre-pattern electrodes, and the use of such substrates during electrodeposition can effect spatially nonconformal material addition by physical constricting deposition to lithographically defined conductive regions.[77–80] To enable spatially defined electrodeposition without a physical template, a semiconductor electrode can be utilized wherein the application of light may activate the deposition and can be modulated to add material in a spatially selective fashion. Semiconductors have conductivities between that of metals and insulators and are characterized by the presence of a band gap energy (E_g), an energy range in which there is no density of electronic states, and a Fermi level energy (E_F), the energy wherein the probability of finding an electron in a metal is 50%, which falls within E_g. The band gap is bookended by the valence and conduction bands which, at absolute zero, are fully occupied with electrons and fully unoccupied, respectively. The band gap is thus the difference in energy between the valence band maxima (E_{VB}) and the conduction band minima (E_{CB}). The band gap energy of most semiconductors is generally characteristic of photons from the near infrared, through the visible, and into the ultraviolet part of the electromagnetic spectrum. Semiconductors are frequently doped with extrinsic impurities to increase carrier concentrations; dopants can either be donors or acceptors of electrons and the resulting materials are referred to a n-type or p-type, respectively. Illumination of a p-type semiconductor with photon energies exceeding E_g moves electrons from the valence band to the conduction band and effects a large number of photogenerated minority carriers. These mobile charge carriers are generated only upon absorption of a photon and have an increased energy relative to electrons in the valence band, and thus can be used to access thermodynamically uphill electrochemical transformations.

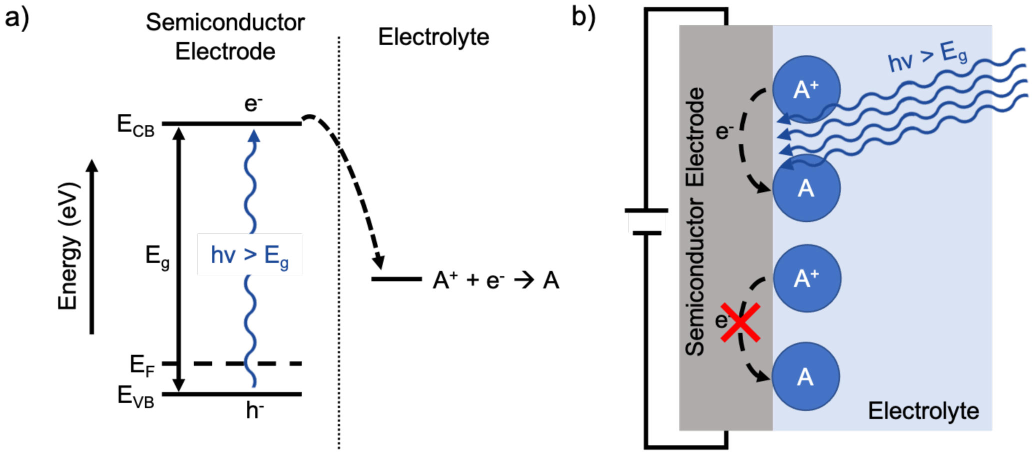

Figure 1.2 (a) Simplified energy diagram for a p-type semiconductor under illumination in contact with electrolyte. Absorption of a photon with energy exceeding E_g generates a mobile charge carrier in the conduction band. The increased energy of this photogenerated electron, relative to E_{VB}, can be used to effect reduction of solution species, A^+. (b) Schematic of cathodic photoelectrodeposition at a semiconductor electrode. Under illumination, photogenerated electrons are available and have sufficient energy to effect material deposition (top) whereas in the dark, mobile charge carriers are not available, and material deposition does not occur (bottom).

Figure 1.2a presents a simplified energy band diagram of a p-type semiconductor under illumination with supra-bandgap energy in contact with an electrolyte and redox active species. Upon absorption of a photon, a pair of photogenerated charge carriers (an electron and a hole) is generated as an electron is excited from the valence band to the conduction band. The energy of the mobile minority carrier is raised above standard reduction potential of species A^+ in solution and thus can be transferred across the solid/liquid interface to effect reductive deposition of species A. Figure 1.2b presents a schematic of a cathodic photoelectrodeposition process at a p-type semiconductor. Light absorption generates mobile minority carriers which have sufficient energy to drive material deposition. In the dark, sufficiently energetic mobile charge carriers are not available and thus deposition does not occur. Thus, photoelectrodeposition can be used to generate spatially-defined material patterning. Spatially inhomogeneous material pattering using structured or rastered illumination has been demonstrated via photoelectrodeposition onto photoactive substrates.[81–87] Additionally, photoelectrodeposition onto structured semiconductors with anisotropic and localized absorption behavior has demonstrated generation of spatially localized deposition profiles which were determined by the optical absorption profiles within the semiconductor.[88,89]

Electrodeposition is inherently complex because the interface where electron transfer occurs constantly evolves as material is added. Intrinsic and extrinsic factors, including but not limited to material microstructure, electrical conductivity, mechanical stresses, surface area, and interfacial roughness, continuously change as deposition proceeds and modulate subsequent electron transfer and associated material addition.[90–95] In the case of light-mediated electrodeposition on a semiconducting substrate, light must reach the substrate to effect the generation of mobile charge carriers, which must then travel to the solid/liquid interface to effect material deposition. As material is added, light absorption at the substrate is blocked by the deposit, and the necessary charge transfer distance between the semiconductor and the interface becomes large, and thus material deposition becomes self-limiting. However, in the case of light-driven electrodeposition of a semiconducting material, absorber material is consistently present at the growth interface and thus light absorption and charge carrier generation can occur far from the substrate. Photoelectrodeposition of semiconductors is therefore not self-limiting and can be used to continuously add material in 3D. Furthermore, illumination of semiconductors during deposition effects increased rates of material deposition relative to those observed in the dark.[96–99] Additionally, the evolving film can impact interfacial light absorption which may influence subsequent material addition, as has been demonstrated in inorganic phototropic growth of Se-Te films.[48–55,100] The specific optical phenomena that lead to structure formation during inorganic phototropic growth will be discussed in detail throughout this thesis.

1.3 Scope of This Thesis

The work discussed in this thesis expands upon previous studies on inorganic phototropic growth, which had previously only been demonstrated in the generation of Se-Te films. Chapter 2 and Chapter 3 examine the use of inorganic phototropic growth to generate mesostructured PbSe and CdSe films, respectively.[101,102] These chapters demonstrate that inorganic phototropic growth is a generalizable process that can be effected with a wide range of semiconductor materials and is not a phenomenon unique to Se-Te. The next chapters explore the generation and evolution of unique and complex mesostructured morphologies via inorganic phototropic growth using Se-Te as a model system. Chapter 4 examines the morphological evolution of mesostructures in response to spectral shifts in illumination conditions during growth.[103] Chapter 5 expands upon Chapter 4 and describes a unique, asymmetric growth response to changes in illumination conditions wherein morphological evolution occurred in one direction of spectral shift but not the other.[104] Chapter 6 demonstrates the generation of Se-Te mesostructures which exhibit periodic order in two orthogonal directions despite use of a single illumination input, and examines the interfacial optical phenomena that effect such structures. Finally, Chapter 7 provides a detailed description of the experimental methods used in the preceding chapters.

Chapter 2

TEMPLATE-FREE SYNTHESIS OF PERIODIC THREE-DIMENSIONAL PBSE NANOSTRUCTURES VIA PHOTOELECTRODEPOSITION

Adapted with permission from: Carim, A. I.*; Hamann, K. R.*; Batara, N. A.; Thompson, J. R.; Atwater, H. A.; Lewis, N. S. Template-Free Synthesis of Periodic Three-Dimensional PbSe Nanostructures via Photoelectrodeposition. *J. Am. Chem. Soc.* **2018**, *140*, 6536–6539. DOI: 10.1021/jacs.8b02931. Copyright 2018 American Chemical Society. *(*equal author contributions)*

2.1 Introduction

In this chapter, the synthesis of PbSe nanostructures via inorganic phototropism, analogous to that previously developed for generation of mesostructured Se-Te films, is described. In bulk and nanocrystalline forms, PbSe exhibits multiple-exciton generation upon single-photon absorption.[105,106] This phenomenon, coupled with a small electronic band gap, has enabled the generation of high-efficiency photovoltaics and high-sensitivity photodetectors with a high responsivity to mid-infrared as well as ultraviolet photons.[107–110] Additionally, PbSe is an effective thermoelectric material.[111] In this chapter, the photoelectrodeposition of Se-Pb films using input illumination sources with varied polarizations and wavelengths is described to evaluate the relation between the optical excitation and the resultant morphology and associated order and anisotropies. Computational modeling of the growth, involving simulations of the light-material interactions during deposition, confirmed the physics of the observed pattern development.

The structured Se-Pb deposits were subsequently electrochemically processed to produce anisotropic, patterned, crystalline PbSe structures.

2.2 Results and Discussion

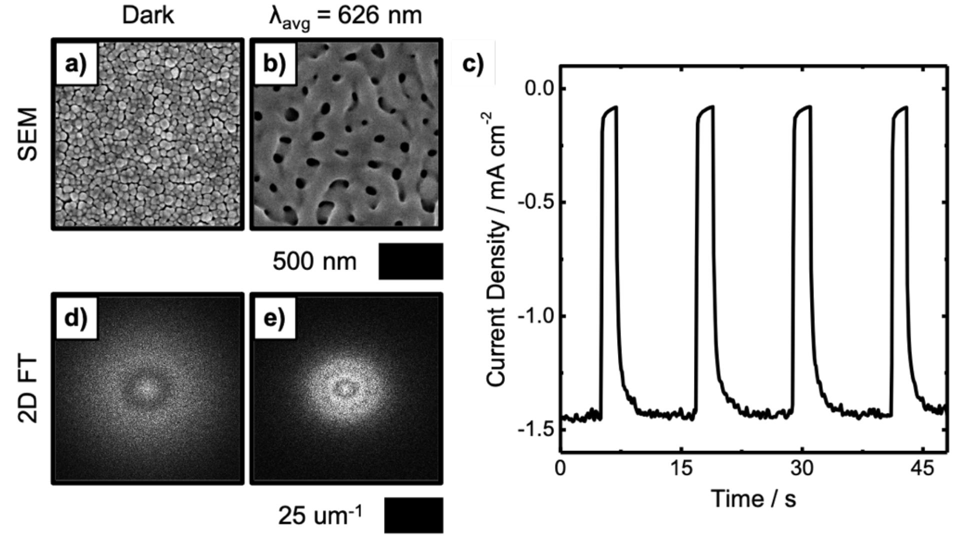

Figure 2.1 (a) and (b) SEMs representative of Se-Pb deposits generated (a) in the dark and (b) using unpolarized $\lambda_{avg} = 626$ nm illumination. (c) Chronoamperometric response under chopped $\lambda_{avg} = 626$ nm illumination for an electrode supporting a photoelectrodeposited Se-Pb film. (d) and (e) 2D FTs generated from SEMs of the deposits depicted in (a) and (b), respectively.

Se-Pb films were electrochemically deposited at room temperature from an aqueous solution of 0.0100 M SeO_2, 0.0050 M $Pb(ClO_4)_2$, and 0.100 M $HClO_4$ onto a Au-coated n^+-Si substrate biased for 10.00 min potentiostatically at 0.00 V versus a Ag/AgCl (3.00 M KCl) reference electrode (additional experimental details provided in Chapter 7). Figure 2.1a presents a representative scanning electron micrograph (SEM) of a deposit generated in the dark, and Figure 2.1b presents a representative SEM of a deposit generated using incoherent, unpolarized illumination from a narrow-band LED source with an intensity-weighted average wavelength (λ_{avg}) of 626 nm. The dark deposit did not exhibit substantial patterning, whereas the photoelectrodeposit displayed a mesh-type morphology that consisted of an isotropic array of nanopores distributed conformally over the entire electrode area (0.50 cm x 0.50 cm). Figure 2.1c presents a chronoamperogram with chopped λ_{avg} = 626 nm illumination for an electrode with a Se-Pb film photoelectrodeposited with the electrochemical conditions detailed above. The sharp decreases in current density correlated with deposition when the illumination source was shuttered; the current densities observed were thus much higher, and indicated enhanced rates of mass addition, under the presence of illumination relative to those in the dark. Figure 2.1d and Figure 2.1e present two-dimensional Fourier transforms (2D FTs) derived from SEM data for the dark deposit and the photoelectrodeposit, respectively. Bright regions in the 2D FT represent a periodic component in the SEM from which the 2D FT was derived. Hence, the distance of a bright area from the center of the 2D FT indicates the frequency of the component, whereas the relative location indicates the direction of the periodicity. Both 2D FTs exhibited annular patterns, indicating a lack of morphological anisotropy. However, the 2D FT of the dark deposit exhibited a large annular radius with a diffuse pattern, whereas the 2D FT pattern of the photoelectrodeposit was contained within a smaller radius and was brighter and more sharply defined. This behavior is consistent with the increased morphological homogeneity and long-range order observed in the photoelectrodeposit relative to the dark deposit (Figure 2.1a,b).

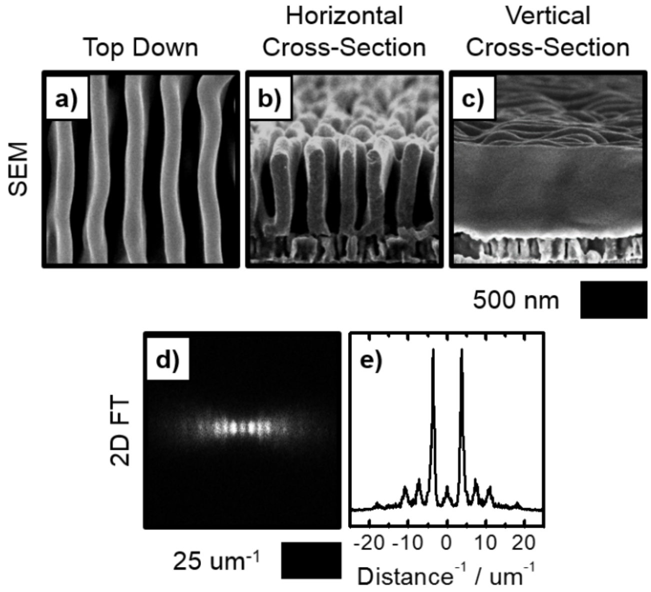

Figure 2.2 (a) Top-down SEM representative of Se-Pb photoelectrodeposits generated with vertically polarized λ_{avg} = 626 nm illumination. (b) and (c) Same as (a) but acquired in cross-section, cleaved along the horizontal, and vertical, axes, respectively. (d) 2D FT generated from a top-down SEM of the deposit depicted in (a). (e) Fourier spectrum derived from the 2D FT in (d).

Figure 2.2a presents a representative top-down SEM of a photoelectrodeposit generated using vertically polarized λ_{avg} = 626 nm illumination. The SEM revealed highly anisotropic lamellar morphologies wherein the long axes of the lamellae were oriented parallel to the polarization axis. This pattern was conformal over the entire electrode area. Figure 2.2b and Figure 2.2c present SEMs of deposits analogous to that presented in Figure 2.2a but which were acquired in cross-sectional view from samples that had been cleaved along the horizontal and vertical axes, respectively. The cross-sectional SEM acquired by cleaving the sample perpendicular to the polarization axis (Figure 2.2b) provides a perspective looking down the lamellar axis and highlights the high aspect ratio of the lamellar features and thus the substantial out-of-plane anisotropy of the photoelectrodeposit. A comparison between this cross-section and that acquired by cleaving the sample parallel to the polarization axis (Figure 2.2c) demonstrates the in-plane morphological anisotropy. Figure 2.2d presents a 2D FT generated from a top-down SEM of the deposit depicted in Figure 2.2a. The 2D FT had a row of spots oriented perpendicular to the polarization axis of the illumination source, confirming that the anisotropic nature of the periodicity correlated with the polarization vector. This anisotropy in the 2D FT is in contrast with the annular pattern observed for the 2D FT derived from SEM data acquired from the photoelectrodeposit generated using unpolarized illumination (Figure 2.1e).

Figure 2.2e presents a Fourier spectrum obtained by integrating the grayscale intensity in the 2D FT in Figure 2.2d along a narrow band through the center and along the horizontal. In the spectrum, the inverse of the lowest-frequency local maximum is equivalent to the lamellar period (the distance between two identical points on two neighboring lamellae). Quantitatively, the lamellar period was 259 ± 8 nm for deposits generated using linearly polarized λ_{avg} = 626 nm illumination. The maxima at higher frequencies were integral multiples of the lowest maximum, and thus are overtones of a single fundamental. This observation is consistent with the contrast in the SEMs (Figure 2.2a,b), suggesting that the topological profile is not perfectly described by a sinusoidal function.

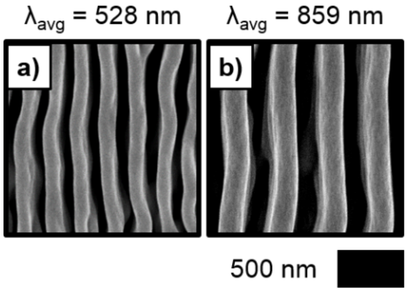

Figure 2.3 (a) and (b) SEMs representative of Se-Pb photoelectrodeposits generated using vertically polarized illumination with the indicated λ_{avg}.

Figure 2.3a and Figure 2.3b present representative SEMs of photoelectrodeposits generated using vertically polarized narrow-band LED sources with λ_{avg} = 528 nm and 859 nm, respectively. Both photoelectrodeposits exhibited an ordered lamellar morphology in which the long axes of the lamellae were oriented vertically. However, the use of λ_{avg} = 528 nm illumination produced smaller lamellar features, with a smaller apparent period, than was observed in photoelectrodeposits formed using λ_{avg} = 626 nm (Figure 2.2a). Similarly, use of λ_{avg} = 859 nm illumination resulted in the generation of larger features with a larger apparent period. Fourier analysis indicated periods of 212 ± 6 nm and 335 ± 16 nm for photoelectrodeposits generated with λ_{avg} = 528 nm and 859 nm illumination, respectively. The control of the Se-Pb photoelectrodeposit morphology observed herein by setting λ_{avg} and the polarization thus definitively confirms that the light-directed deposition technique is not limited to Se-Te alloys, but is a more general property of the interactions between light and matter.

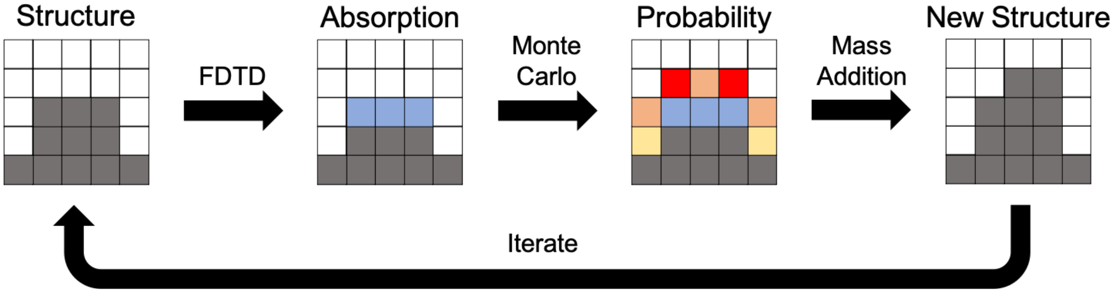

Figure 2.4 Schematic of optically-based growth simulation used to model inorganic phototropic growth. First, light absorption was calculated using full-wave finite-difference time-domain electromagnetic simulations. A Monte Carlo method was then used to add mass probabilistically based on absorption data calculated in the previous step. The process was iterated to simulate growth.

Computer simulations of the growth were performed to evaluate the physics underlying the formation of the observed photoelectrodeposit nanopatterns. A two-step iterative model was utilized and is presented schematically in Figure 2.4. Full-wave finite-difference time-domain (FDTD) electromagnetic simulations were first used to calculate the local photocarrier-generation rates at the growth interface (full modeling and simulation details are described in Chapter 7).[48,52] Electrochemical mass addition was then simulated via a Monte Carlo method that used these generation rates to weight the local mass-addition probability. No empirical data were used in the model other than estimates of the complex index of refraction, charge-carrier concentrations, and excited-state lifetimes of the Se-Pb material. The computational results are therefore fully a consequence of the fundamental light-material interactions during growth.

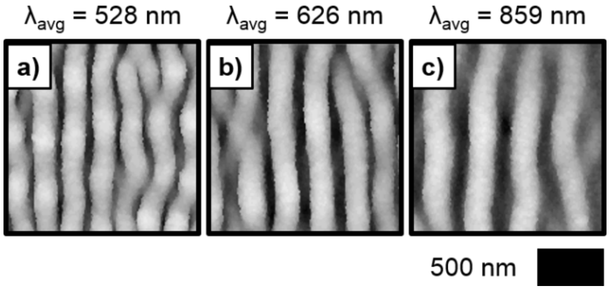

Figure 2.5 (a) – (c) Simulated Se-Pb photoelectrodeposit morphologies generated using vertically polarized illumination with the indicated λ_{avg}.

Figure 2.5 presents simulated morphologies for photoelectrodeposition using vertically polarized sources with λ_{avg} = 528 nm (Figure 2.5a), 626 nm (Figure 2.5b), and 859 nm (Figure 2.5c). Inspection of these simulated structures indicates excellent agreement with the observed SEM data (Figure 2.3a, Figure 2.2a and Figure 2.3b). The simulations had lamellar periods of 225 ± 10 nm, 253 ± 10 nm and 321 ± 12 nm for deposition with λ_{avg} = 528 nm, 626 nm, and 859 nm, illumination, respectively. These periods are quantitatively in accord with the actual SEM data, confirming that the nanopatterning is directed by the light-matter interactions during deposition and is principally defined by the specific illumination utilized.

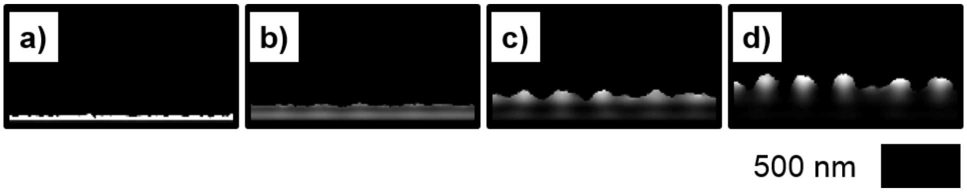

Figure 2.6 (a) – (d) Simulated cross-sectional light absorption profiles for successive stages of Se-Pb photoelectrodeposition using polarized λ_{avg} = 626 nm illumination.

Figure 2.6 presents simulated cross-sectional light absorption profiles, generated using the iterative growth model, for successive stages of photoelectrodeposition using polarized λ_{avg} = 626 nm illumination. Initially, the absorption magnitude was spatially conformal across the surface as the incident illumination was unstructured (Figure 2.6a). However, roughness developed, due to the random nucleation of the electrodeposited material, and effected scattering of the incident illumination and non-uniform absorption (Figure 2.6b). Locally elevated light absorption drives locally accelerated rates of material deposition. The evolving surface continued to scatter incident illumination, and interference of the scattered light resulted in a spatially oscillating absorbance (Figure 2.6c). A periodic lamellar structure emerged wherein absorption was concentrated in the structure tips, resulting in sustained anisotropic growth (Figure 2.6d).

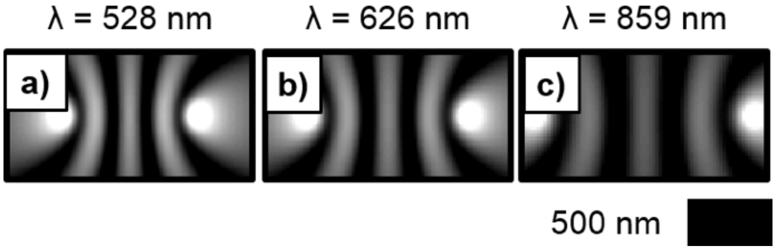

Figure 2.7 (a) – (c) Simulations of normalized time-average E-field magnitudes from two dipoles emitting radiation with indicated free-space wavelengths in a medium of index n = 1.33 and separated by a distance of two wavelengths perpendicular to the oscillation axis.

Point dipole sources were used to model the amplitude of the electric field (E-field) modulation at the nascent growth interface caused by scattering of the incident illumination by the roughness effected by random nucleation of electrodeposited material. Figure 2.7 presents FDTD simulations of normalized time-averaged E-field magnitudes from two dipoles emitting radiation with free-space wavelengths of $\lambda = 528$ nm (Figure 2.7a), 626 nm (Figure 2.7b), and 859 nm (Figure 2.7c), in a medium of index $n = 1.33$ and separated by a distance of two wavelengths perpendicular to the oscillation axis. In each case, interference fringes are observed. The spacing and width of the fringes were proportional to the wavelength. These data are consistent with the observation of increasing lamellar periods and features sizes with increasing values of λ_{avg}.

The modeling of the initial light scattering at the growth interface using dipole sources (Figure 2.7), along with the simulated light absorption profiles for successive stages of the photoelectrodeposition process generated using the iterative growth model (Figure 2.6), together indicate that the fundamental light-matter interactions that optically direct the growth process are principally constrained to the interplay between the deposited material and the incident illumination and are independent of the underlying substrate. The light scattering simulations suggest that a spatially oscillating light intensity pattern can be generated from scattering off of electrodeposit nuclei, and the light absorption profiles indicate that the incident illumination is strongly absorbed and attenuated by the tips of the deposited structure.

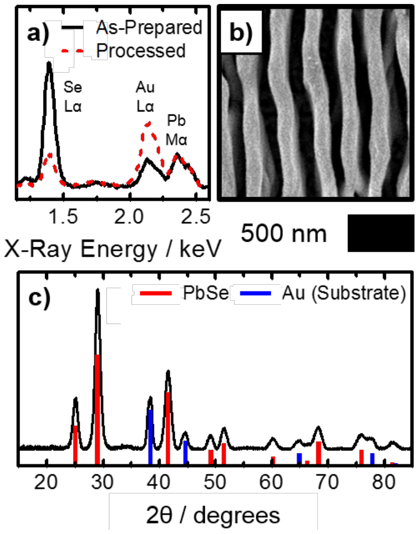

Figure 2.8 (a) EDX spectra acquired from a Se-Pb photoelectrodeposit generated with vertically polarized λ_{avg} = 626 nm illumination as-prepared and after processing by cathodic polarization in 0.500 M $H_2SO_{4(aq)}$. Representative (b) SEM and (c) GIXRD pattern of a Se-Pb photoelectrodeposit generated with vertically polarized λ_{avg} = 626 nm illumination after processing by cathodic polarization in 0.500 M $H_2SO_{4(aq)}$.

Figure 2.8a presents energy-dispersive X-ray (EDX) spectra acquired from a photoelectrodeposit generated with vertically polarized λ_{avg} = 626 nm illumination. The solid trace corresponds to the as-deposited sample and contains Se Lα and Pb Lα signals that originated from the photoelectrodeposit, in addition to a Au Lα signal from the substrate. Quantification of the EDX data indicated that the as-deposited Se-Pb films had a 3 : 1 Se : Pb atomic ratio. To produce stoichiometric PbSe, after growth the photoelectrodeposits were transferred to 0.500 M $H_2SO_{4(aq)}$ and were biased cathodically, thereby effecting reductive elimination of excess Se.[112,113] The dashed trace in Figure 2.8a presents an EDX spectrum of a photoelectrodeposit after cathodic polarization. A decrease in the intensity of Se Lα signal was observed relative to the spectrum of the as-prepared deposit, and quantification revealed a 1 : 1 Se : Pb atomic ratio. Figure 2.8b presents a representative SEM of a photoelectrodeposit generated with vertically polarized λ_{avg} = 626 nm illumination after cathodic polarization. After removal of excess Se, an anisotropic, periodic lamellar-type pattern was observed with a nearly-identical period (255 ± 6 nm), diminished feature size, and increased surface texture, relative to the as-prepared material. Figure 2.8c presents a grazing-incidence X-ray diffraction (GIXRD) pattern acquired from a processed photoelectrodeposit similar to that depicted in Figure 2.8b and shows reflections consistent with polycrystalline PbSe. Photoelectrodeposition coupled with an electrochemical post-processing step can thus enable the template-free generation of highly anisotropic and ordered three-dimensional PbSe nanostructures.

2.3 Conclusions

In summary, photoelectrochemical growth yielded spontaneous, template-free pattern formation of highly ordered, periodic Se-Pb nanostructures, with the specific deposit morphologies determined by the nature of the illumination during growth. The use of unpolarized illumination resulted in the generation of an isotropic mesh-type pattern, whereas linearly polarized illumination generated a highly anisotropic, lamellar-type pattern wherein the long axes of the lamellae were oriented parallel to the polarization axis. The lamellar feature size and period scaled proportionately with λ_{avg}. Computer modeling of the growth process based on simulations of the fundamental optical phenomena at the growth interface accurately reproduced the experimentally observed morphologies, and quantitatively matched the empirical lamellar period, confirming that the observed patterns are a consequence of the fundamental light-material interactions during growth. SEM, EDX, and GIXRD analysis collectively indicated that cathodic polarization of the Se-Pb structures in $H_2SO_{4(aq)}$ provided a facile, general method to produce patterned nanostructures of stoichiometric, polycrystalline PbSe.

Chapter 3

OPTICALLY TUNEABLE CDSE MORPHOLOGIES VIA INORGANIC PHOTOTROPIC GROWTH

Hamann, K. R.*; Carim, A. I.*; Meier, M. C.; Thompson, J. R.; Batara, N. A.; Yermolenko, I. S.; Atwater, H. A.; Lewis, N. S. Optically Tunable Mesoscale CdSe Morphologies via Inorganic Phototropic Growth. *J. Mater. Chem. C* **2020**, *8*, 12412–12417. DOI: 10.1039/D0TC02126A.

3.1 Introduction

In this chapter, the generation and control of mesostructured morphologies of an important semiconductor material, CdSe, via inorganic phototropic growth is described. CdSe is a direct bandgap semiconductor with an absorption edge in the visible region of the electromagnetic spectrum. Substantial effort has been directed towards controlling the crystal habit and morphology of colloidally synthesized CdSe nanocrystals via the use of chemical directing agents.[114–116] Mesostructured CdSe films have been fabricated by numerous methods on solid substrates using solution-grown nanoparticles, including the use of ligand-directed assembly, infilling of solid supports, and polymer encapsulation.[117–119] Structured CdSe films have also been generated via electrochemical deposition into physical templates.[120,121] CdSe films generated via both colloidal and electrochemical routes are being studied extensively for many applications including use as photodetectors, solar light absorbers, and light-emitters.[122–127] Herein, inorganic phototropic growth was used to generate mesostructured Se-Cd films. Growth was performed using spatially conformal illumination with varying input wavelengths and polarizations, and the morphological outcomes were assessed as functions of the characteristics of the optical inputs. The growth process was modeled using simulations of the optical processes at the growth interface, confirming the interactions that directed the mesoscale morphological evolution. The Se-Cd films were then processed via immersion in $CS_{2(l)}$, to produce stoichiometric, polycrystalline CdSe mesostructures over macroscopic areas (i.e. an entire electrode substrate).

3.2 Results and Discussion

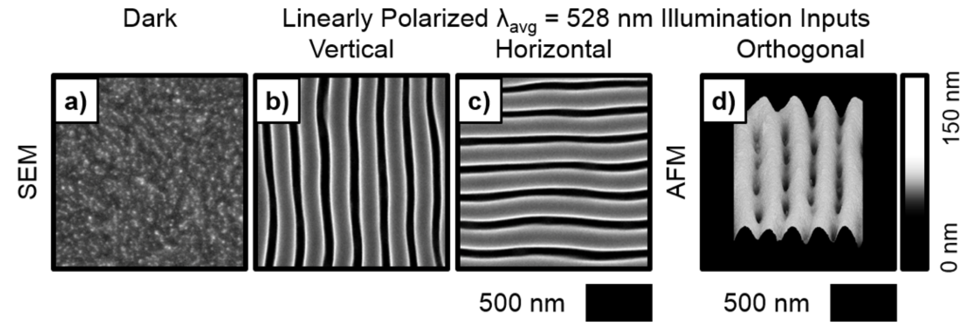

Figure 3.1 SEMs representative of Se-Cd films generated (a) in the dark and using (b) vertically polarized, and (c) horizontally polarized, λ_{avg} = 528 nm illumination. (d) Perspective-view AFM representative of a Se-Cd film generated by inorganic phototropic growth in a single step using two orthogonally polarized λ_{avg} = 528 nm illumination inputs (a 0.7 fraction of the total intensity was provided in one polarization and the balance in the orthogonal polarization).

Se-Cd films were electrochemically grown on Au-coated n^+-Si substrates from an aqueous solution of 0.00500 M SeO_2, 0.200 M $CdSO_4$, and 0.100 M H_2SO_4 (additional experimental details provided in Chapter 7). Figure 3.1a presents a representative SEM of a film grown in the dark, showing a lack of ordered surface texture. In contrast, Figure 3.1b presents a representative SEM of a film grown under incoherent illumination from a LED source with λ_{avg} = 528 nm and polarized linearly with the E-field vector aligned along the vertical. No far-field spatial manipulation of the light field was utilized, and the same intensity, wavelength, and linear polarization was delivered to each point of substrate, yet the film displayed a sharply defined, highly anisotropic, periodic ridge and trench nanotexture, with features oriented vertically and generated conformally over the entire surface of the macroscopic substrate (0.50 cm x 0.50 cm). Figure 3.1c presents a representative SEM of a film grown in a similar manner to that presented in Figure 3.1b but with the illumination polarized such that the E-field vector aligned horizontally, revealing a similar nanotexture but with horizontally oriented features. Figure 3.1d presents a representative atomic force micrograph (AFM) of a film grown using simultaneous illumination from two orthogonally polarized λ_{avg} = 528 nm LED sources with non-equal intensities. The micrograph depicts the full three-dimensional topography, as well as cross-sectional profile, of the film produced under these illumination conditions. This intricate three-dimensional morphology exhibited an anisotropic, periodic ridge and trench nanotexture similar to that observed with a single polarized illumination input (Figure 3.1b,c), but with an additional shorter intersecting ridge and trench motif having features that were periodic in the direction orthogonal to the periodicity of the taller motif. The observation of two morphological components with orthogonal periodicities correlates with the use of two orthogonally polarized optical inputs during the single growth process step.

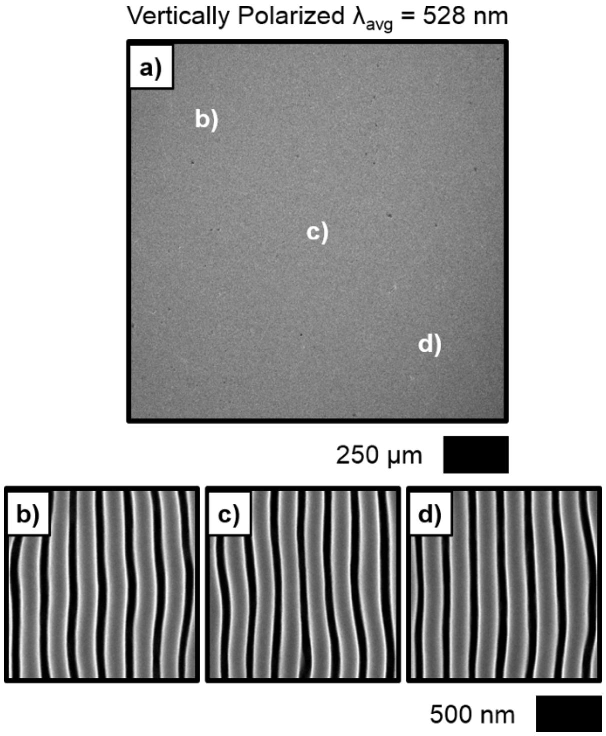

Figure 3.2 (a) Low-magnification SEM of a Se-Cd film generated using vertically polarized λ_{avg} = 528 nm illumination. (b) – (d) High-magnification SEMs acquired from the areas indicated in the SEM presented in (a).

Figure 3.2a presents a low-magnification SEM of a Se-Cd film generated via inorganic phototropic growth using λ_{avg} = 528 nm. Figure 3.2b–d presents high-magnification SEMs of the same sample, taken from the areas indicated in Figure 3.2a. The morphologies observed in Figure 3.2b, Figure 3.2c, and Figure 3.2d were consistent with one another: a vertically oriented ridge and trench nanotexture, with a well-defined feature width and periodicity, was observed in each case. These data highlight the potential of the inorganic phototropic growth technique to readily generate over macroscopic areas, in a single scalable process step with unstructured illumination and an unstructured substrate, surfaces having the three-dimensional structure necessary to mimic those observed in purpose-evolved biological interfaces.[42,128] Scaling of the process to generate such surfaces over large macroscale areas may be accomplished simply by use of illumination that conformally fills the target region. Inorganic phototropic growth does not require use of coherent nor monochromatic illumination: any incandescent, LED, or laser sources, as well as sunlight, could provide light input at the requisite scale.[50]

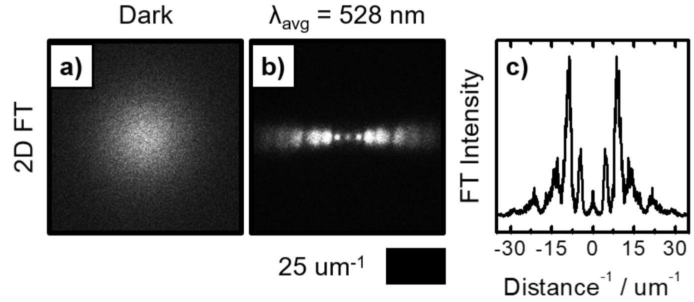

Figure 3.3 2D FTs derived from SEMs of Se-Cd films generated (a) in the dark and using (b) vertically polarized λ_{avg} = 528 nm illumination. (c) Fourier spectrum derived from the 2D FT in (b).

Figure 3.3a and Figure 3.3b present 2D FTs derived from SEM data for each of the films depicted in Figure 3.1a and Figure 3.1b, respectively. Brightness in each 2D FT is indicative of the periodic components in the micrograph from which the 2D FT data were derived. The distance from the center is representative of the component frequency, and the direction relative to the center is the direction of periodicity. The film grown in the dark (Figure 3.1a) exhibited a broad and diffuse circular 2D FT profile (Figure 3.3a), consistent with the isotropic and unpatterned film morphology. The Se-Cd film grown using vertically polarized illumination (Figure 3.1b) exhibited a 2D FT profile characterized by a tight, narrow band of well-defined spots aligned along the horizontal (Figure 3.3b), consistent with the highly anisotropic and ordered nature of the phototropically grown film. These data indicate that the nanotexture periodicity was generated only in the direction perpendicular to the E-field vector of the illumination during growth. Figure 3.3c presents a Fourier spectrum obtained by integrating the grayscale intensity through the horizontal centerline of the 2D FT for the film grown using vertical polarization (Figure 3.3b). The Fourier spectrum revealed a single family of related components consisting of a fundamental frequency along with several higher frequency overtones. The inverse of the fundamental frequency is equivalent to the period of the ridge and trench nanotexture (e.g. distance between identical points on two neighboring ridges). The morphological period was 214 ± 3 nm for films grown using linearly polarized λ_{avg} = 528 nm illumination. The presence of the overtones in the Fourier spectrum indicates that the topological profile of the surface texture in the films does not conform precisely to a sinusoidal profile. The substantial overtone intensity is consistent with the sharp in-plane morphological contrast of the surface texture, indicating that inorganic phototropic growth can effect substantial in-plane anisotropy in the absence of anisotropic or structured illumination inputs.

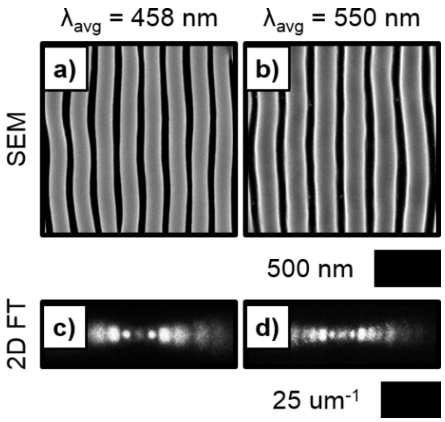

Figure 3.4 (a) and (b) SEMs representative of Se-Cd films generated by inorganic phototropic growth using vertically polarized illumination with the indicated λ_{avg}. (c) and (d) 2D FTs generated from SEMs of the films depicted in (a) and (b), respectively.

Figure 3.4a and Figure 3.4b present representative SEMs of films generated by inorganic phototropic growth using vertically polarized LED sources with $\lambda_{avg} = 458$ and 550 nm, respectively. Use of either illumination source during growth effected nanotextures that exhibited vertically oriented, anisotropic features similar to those observed using vertically polarized $\lambda_{avg} = 528$ nm illumination (Figure 3.1b). The use of $\lambda_{avg} = 458$ nm illumination (Figure 3.4a) resulted in the generation of a smaller feature size and smaller apparent morphological period than when $\lambda_{avg} = 528$ nm (Figure 3.1b) was used, whereas use of $\lambda_{avg} = 550$ nm illumination (Figure 3.4b) resulted in a larger feature size and a larger apparent morphological period, indicating that both the feature size and period are controlled by the λ_{avg} of the illumination during inorganic phototropic film growth. Figure 3.4c and Figure 3.4d present 2D FTs derived from SEM data of films generated with vertically polarized $\lambda_{avg} = 458$ and 550 nm illumination, respectively. Both sets of data were qualitatively similar to the 2D FT data derived from films produced by growth using $\lambda_{avg} = 528$ nm (Figure 3.3b).

The spots in the 2D FTs for λ_{avg} = 458 and 550 nm (Figure 3.4c and Figure 3.4d) were spaced further apart, and closer together, respectively, than for λ_{avg} = 528 nm (Figure 3.3b), consistent with the respective smaller and larger morphological periods apparent in the SEM data (Figure 3.4a and Figure 3.4b) of those systems. Further analysis of the 2D FT data revealed only a single fundamental frequency and associated overtones in each case, suggesting that each value of λ_{avg} encodes for a singular period in the film morphology. Quantitatively, the Fourier analysis indicated periods of 184 ± 4 nm and 230 ± 3 nm for Se-Cd films generated using λ_{avg} = 458 and 550 nm, respectively.

The nanotextures produced by inorganic phototropic growth were hypothesized to be an emergent phenomenon that is a consequence of spatially varying deposition rates resulting from anisotropic coupling between the growing film and the incident illumination. Electromagnetic simulations of the growth process were therefore performed to validate this mechanism of nanotexture formation. A two-step iterative model, similar to that described in Chapter 2 and depicted schematically in Figure 2.4 was used (full modeling details provided in Chapter 7) in which the spatially dependent photocarrier generation rates at the growth interface were first calculated using full-wave electromagnetic simulations. A Monte Carlo method was then used to simulate light-motivated electrochemical growth, with the probability of local mass addition weighted by the local photocarrier generation rate. Empirical inputs to the model were minimal and included estimates of the real and imaginary parts of the complex refractive index of the electrochemically grown material. The results of the model are thus principally defined by the light-matter interactions at the growth interface.

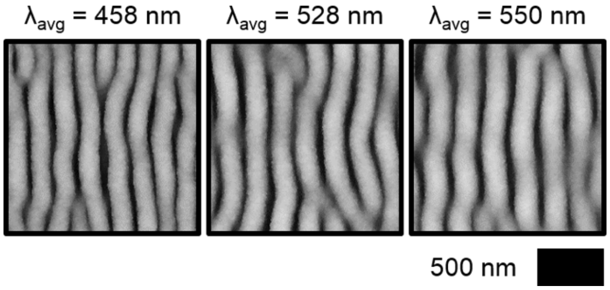

Figure 3.5 Simulated morphologies of Se-Cd films generated by inorganic phototropic growth using vertically polarized illumination with the indicated λ_{avg}.

Figure 3.5 presents simulated morphologies for inorganic phototropic growth using vertically polarized illumination with λ_{avg} = 458, 528, and 550 nm. In each case, vertically oriented, periodic and anisotropic ridge and trench nanotextures were produced with spatial characteristics in close accord with the analogous experimental SEM data for such films (Figure 3.4a, Figure 3.1b, and Figure 3.4b). The characteristic morphological period of the films as determined by FT analysis was 195 ± 8 nm, 219 ± 10 nm, and 230 ± 11 nm for simulations using λ_{avg} = 458, 528, and 550 nm illumination, respectively, thus quantitatively agreeing with the experimental observations of Se-Cd film growth. This agreement, given the optical basis of the model, confirms that the film morphology is a function of the optical characteristics of the photoelectrochemically prepared material and also indicates that observed mesostructure development is primarily instructed by spatially-varying photocarrier generation rather than photothermal and related physical phenomena. Additionally, the simulation data, given the limited empirical input parameters, along with the empirical results, suggests that inorganic phototropic growth is not uniquely demonstrable in the case of a singular, discrete material but rather may be observed in broad range of materials with suitable intrinsic optoelectronic properties.

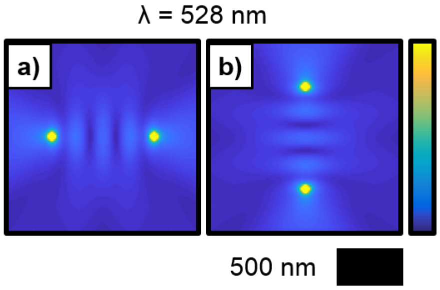

Figure 3.6 Normalized time-average of the E-field magnitude from two dipoles emitting radiation with a free-space wavelength of λ = 528 nm in a medium of refractive index n = 1.33. Dipoles separated by a distance of twice the wavelength (a) along the horizontal and (b) along the vertical with the oscillation axis perpendicular to the axis of separation.

Additional simulations were performed to explore the fundamental optical interactions that underpin the nanotexture formation. The interfacial modulation of the E-field during growth, created by light scattering due to the inherent roughness of the evolving film, was modeled using dipole emission sources. Figure 3.6a presents the normalized time-average of the E-field magnitude from two dipoles emitting with a free-space wavelength of λ = 528 nm in a medium of index $n = 1.33$ (representative of the growth solution), separated by a distance of two wavelengths along the horizontal, and with the E-field oscillation axis along the vertical. A parallel set of vertically oriented interference fringes was observed between the dipoles, analogous to the ridge and trench nanotexture that was generated experimentally with inorganic phototropic growth using vertically polarized illumination (Figure 3.1b). Figure 3.6b presents a similar dipole simulation in which the separation and oscillation axes were along the vertical and the horizontal, respectively. Analogous interference fringes were observed, but oriented horizontally, analogous to the orientation of the nanotexture observed experimentally when horizontally polarized illumination was used (Figure 3.1c). The interference is thus hypothesized to promote the growth of the observed ordered nanotextures by producing a spatially varying, periodic near-field light intensity profile.

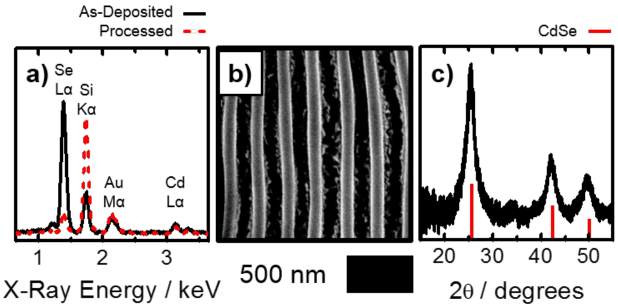

Figure 3.7 (a) Representative EDX spectra acquired from a Se-Cd film grown with vertically polarized λ_{avg} = 528 nm illumination as-deposited and after chemical processing with $CS_{2(l)}$. Representative (b) SEM and (c) GIXRD pattern of a Se-Cd film grown with vertically polarized λ_{avg} = 528 nm illumination after chemical processing with $CS_{2(l)}$.

Figure 3.7a presents representative EDX spectra acquired from films grown using vertically polarized λ_{avg} = 528 nm illumination. The solid black trace corresponds to the as-deposited material, and exhibits Se Lα and Cd Lα signals from the deposit as well as Si Kα and Au Mα signals from the substrate. Quantification of the EDX data indicated a Se : Cd atomic ratio of 6 : 1. The as-deposited sample was then chemically processed by immersion in $CS_{2(l)}$ under reflux at ~ 46° C, to dissolve excess Se and yield stoichiometric CdSe.[129,130] The dashed red trace in Figure 3.7a corresponds to an EDX spectrum of a film after processing with $CS_{2(l)}$, with quantification indicating a 1 : 1 Se : Cd atomic ratio. Figure 3.7b presents a representative SEM of a chemically processed film that was initially grown using vertically polarized λ_{avg} = 528 nm illumination. After processing, an ordered mesoscale morphology consisting of a ridge and trench nanotexture was observed with a reduced feature size and slightly increased period (227 ± 2 nm) relative to the as-deposited film resulting from the removal of excess Se mass. Figure 3.7c presents a GIXRD pattern acquired from a processed film similar to that depicted in Figure 3.7b. The GIXRD pattern displayed characteristic reflections indicative of polycrystalline CdSe. Thus, inorganic phototropic growth coupled with a low-temperature solution processing step effected the generation of CdSe films with highly ordered mesoscale morphologies that can be tailored via manipulation of the characteristics of the illumination during growth.

3.3 Conclusions

In summary, inorganic phototropic growth of Se-Cd via an optically-directed electrochemical method using an isotropic aqueous solution, conformal unstructured illumination, and no physical or chemical templating agents, resulted in the generation of films that exhibited highly ordered and precise three-dimensional mesoscale morphologies. Growth in the dark resulted in films with no observable ordered nanotexture whereas growth using linearly polarized illumination resulted in films exhibiting controllable, periodic, and anisotropic ridge and trench nanotextures over macroscopic areas. The characteristics of the film morphology were controlled by the illumination, with the in-plane direction of the nanotexture anisotropy and periodicity set by the input E-field vector and with a morphological period that scaled with the input λ_{avg}. Modeling of the inorganic phototropic growth process based on full-wave electromagnetic simulations of the interfacial optical interactions closely reproduced the experimentally observed nanotextures, including quantitative agreement with the observed morphological periods, indicating that nanotexture development is a product of the light-matter interactions during growth. Additional modeling of the interfacial light scattering also supported the hypothesis that the film characteristics were determined principally by optical processes. Solution-phase processing of the as-deposited Se-Cd films in $CS_{2(l)}$ was used to produce stoichiometric, polycrystalline CdSe films with ordered, anisotropic nanotextures and controlled three-dimensional morphologies, demonstrating a scalable, high-throughput technique to prepare structured CdSe films over macroscale areas. The cumulative data suggest that inorganic phototropic growth may be extendable to generate precise mesostructures in a range of semiconducting materials, including constituents of the II-VI family of materials. Furthermore, the feature sizes, anisotropies, and pattern fidelities, as well as the macroscale conformality, of the morphologies generated in this work by inorganic phototropic growth resemble numerous environmentally facing biological interfaces with evolutionarily defined physical purposes. For example, butterfly wings exhibit nanoscale lamellar structures that produce defined structural coloration which provides superior visibility relative to pigmentary coloration, as well as possessing characteristics such as superhydrophobicity that enable anisotropic dewetting.[131,132] Inorganic phototropic growth may thus provide a route towards the scalable, bottom-up generation of biomimetic materials with unique and potentially useful physical properties derived from complex but controllable mesoscopic interfacial structure.

Chapter 4

PLASTIC MORPHOLOGICAL RESPONSE TO SPECTRAL SHIFTS DURING INORGANIC PHOTOTROPIC GROWTH

Adapted with permission from: Hamann, K. R.; Meier, M. C.; Lewis, N. S.; Carim, A. I. Plastic Morphological Response to Spectral Shifts during Inorganic Phototropic Growth. *JACS Au* **2022**, *2*, 865–874. DOI: 10.1021/jacsau.1c00588. Copyright 2022 American Chemical Society.

4.1 Introduction

The preceding chapters focused on exploring inorganic phototropic growth in material systems beyond Se-Te. This chapter will explore specific morphological evolutions during inorganic phototropic growth with dynamic illumination inputs. Here, Se-Te will be used, as the growth process has been well-described, and it thus serves as an ideal model system to study fundamental growth behavior in response to complex illumination conditions. In this chapter, morphological plasticity in response to a change in the input wavelength during inorganic phototropic growth is explored in detail. Deposition was effected in a two-step process using a series of different LEDs with discrete output wavelengths ($\lambda_0 \neq \lambda_1$), and the resulting morphologies were evaluated by SEM and Fourier analysis. Changes in illumination wavelength from λ_0 to λ_1 produced deposit structural evolution including feature branching, termination, and/or fusion along the growth direction such that the interfacial feature pitch eventually matched that obtained for growth using only λ_1. Modeling of the deposition was performed by considering the light-material interactions at the growth interface, and further optical simulations were used to examine the mechanism of the plastic response. These simulations revealed interfacial light scattering and concentration behavior that directed the photomorphogenesis.

4.2 Results and Discussion

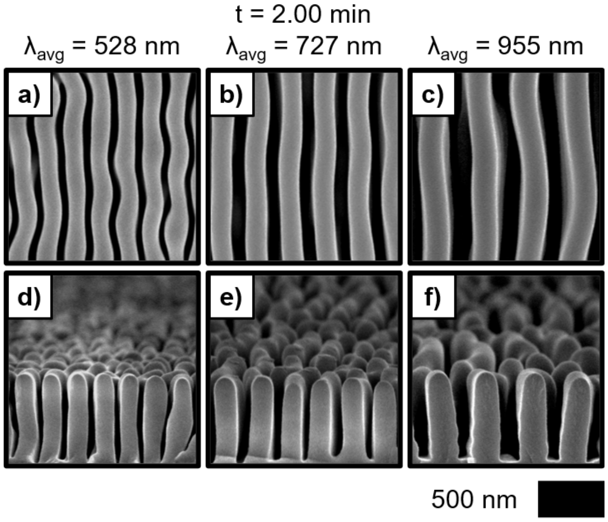

Figure 4.1 (a) – (c) Representative top-down and (d) – (f) cross-sectional SEMs of Se-Te deposits generated using the indicated λ_{avg} illumination for $t = 2.00$ min.

Se-Te films were grown from an aqueous solution of oxidized precursors by light-mediated electrodeposition using unstructured, vertically polarized illumination from low-power, narrowband LED sources. Figure 4.1a–c presents representative top-down SEMs of films deposited for $t = 2.00$ min using the specified λ_{avg}. Highly anisotropic and periodic lamellar features were observed in which the long axes of the lamellae were oriented vertically, parallel to the input polarization vector. Feature width and pitch were observed to scale with λ_{avg}. 2D FT analysis of top-down SEM data was used to quantify the morphological periods and values of 203 ± 6, 263 ± 6, and 371 ± 6 nm were measured for films generated by deposition for t = 2.00 min using λ_{avg} = 528, 727, and 955 nm, illumination, respectively (Λ_{528}, Λ_{727}, and Λ_{955}). Figure 4.1d–f presents representative cross-sectional SEMs, complementary to the top-down data presented in Figure 4.1a–c, that were obtained by cleaving films perpendicular to the direction of the input polarization vector. The lamellar features projected along the substrate normal axis and exhibited substantial out-of-plane anisotropy.

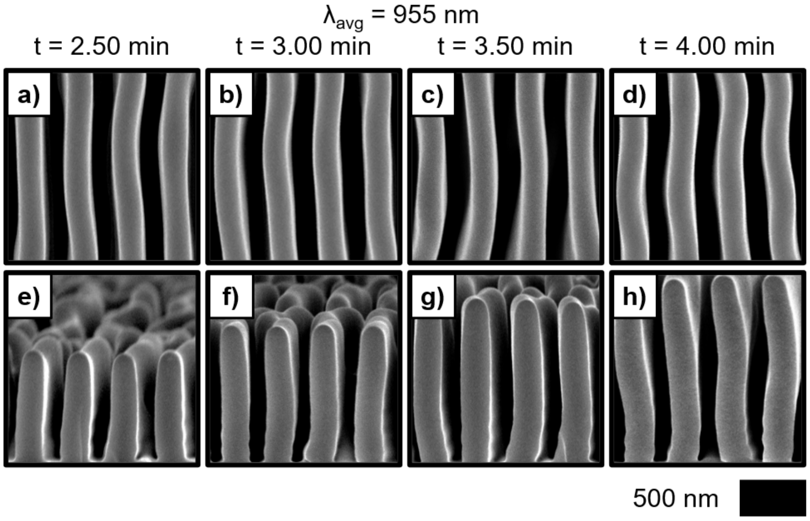

Figure 4.2 (a) – (d) Representative top-down and (e) – (h) cross-sectional SEMs of deposits generated using λ_{avg} = 955 nm for the indicated t.

Figure 4.2 presents top-down (Figure 4.2a–d) and cross-sectional (Figure 4.2e–h) SEMs of films deposited using a constant illumination source with λ_{avg} = 955 nm. The features were observed to increase in height with increasing growth time (Figure 4.2e–h) without a change in the in-plane, interfacial morphology (Figure 4.1a–d), indicating that feature extension occurred linearly along the out-of-plane direction for constant illumination with a single, unchanging wavelength.

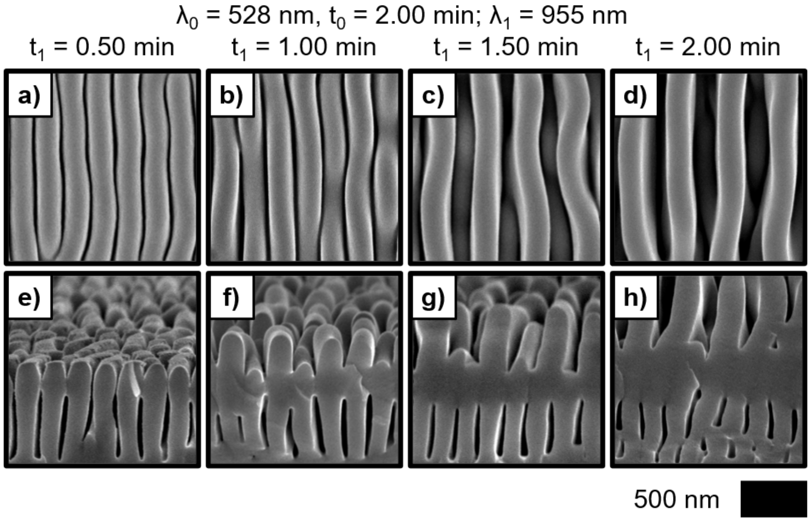

Figure 4.3 (a) – (d) Representative top-down and (e) – (h) cross-sectional SEMs of deposits generated initially using λ_0 = 528 nm for t_0 = 2.00 min, and then extended in a subsequent deposition step using λ_1 = 955 nm for the indicated t_1.

Figure 4.3 presents representative top-down (Figure 4.3a–d) and cross-sectional (Figure 4.3e–h) SEMs of films that were initially deposited for t_0 = 2.00 min using $\lambda_{avg} = \lambda_0 = 528$ nm illumination (Λ_{528}) and were subsequently, in a second deposition step, extended using $\lambda_{avg} = \lambda_1 = 955$ nm illumination for the indicated time, t_1. At t_1 = 0.50 min, an increased feature width was observed (Figure 4.3a) relative to that for Λ_{528} (Figure 4.1a). Near the tips of the lamellae, deposition occurred in the space between adjoining lamellae, bridging some features (Figure 4.3e). Further deposition using λ_1 resulted in non-uniform feature heights (Figure 4.3b); cross-sectional analysis revealed an oscillatory height profile in which approximately every other lamella was extended along the substrate normal but the interspersed features exhibited little growth (Figure 4.3f). At t_1 = 1.50 min, the top-down SEM data revealed a substantial decrease in the interfacial feature density and a concomitant increase in the width of the remaining features (Figure 4.3c). In accord, the cross-sectional SEM data showed the termination of every second feature defined by the initial deposition with λ_0 (Figure 4.3g). 2D FT analysis indicated that the interfacial period of the growing structures increased from 262 ± 10 nm for t_1 = 1.00 min to 316 ± 12 nm for t_1 = 1.50 min. Additional deposition using λ_1 = 955 nm resulted in extension of the remaining features along the substrate normal axis (Figure 4.3d,h) and an interfacial period of 361 ± 6 nm for t_1 = 2.00 min, consistent with the interfacial period obtained for Λ_{955}.

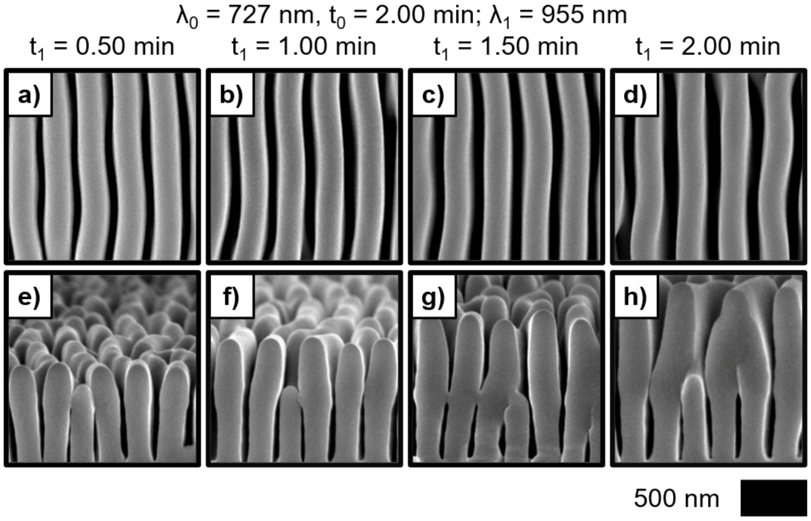

Figure 4.4 (a) – (d) Representative top-down and (e) – (h) cross-sectional SEMs of deposits generated initially using λ_0 = 727 nm for t_0 = 2.00 min, and then extended in a subsequent deposition step using λ_1 = 955 nm for the indicated t_1.

Figure 4.4 presents representative top-down (Figure 4.4a–d) and cross-sectional (Figure 4.4e–h) SEMs of Λ_{727} films that were extended in a second deposition step using λ_1 = 955 nm for the indicated t_1. After the input wavelength was changed, a larger interfacial feature width was observed (Figure 4.4a) relative to that for Λ_{727} (Figure 4.1b). Cross-sectional analysis revealed that some features exhibited shorter heights than others (Figure 4.4e). At t_1 = 1.00 min, a decrease in the in-plane feature density was observed (Figure 4.4b); 2D FT analysis indicated an interfacial period of 301 ± 6 nm. Cross-sectional analysis showed that some lamellae had terminated whereas others continued to grow linearly along the substrate normal (Figure 4.4f). Additional deposition using λ_1 = 955 nm further decreased the in-plane feature density (Figure 4.4c,d), with the period increasing from 313 ± 6 nm at t_1 = 1.50 min to 331 ± 6 nm at t_1 = 2.00 min. Additional attenuation of features was observed during this stage of growth, and the lamellae that were adjacent to termination sites exhibited transitory growth towards attenuated features in a direction away from the substrate normal, and then again grew along the normal (Figure 4.4g,h).

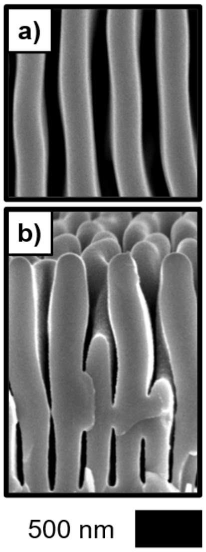

Figure 4.5 (a) Representative top-down and (b) cross-sectional SEMs of deposits generated initially using $\lambda_0 = 727$ nm for $t_0 = 2.00$ min, and then extended using $\lambda_1 = 955$ nm for $t_1 = 3.50$ min.

Figure 4.5 presents top-down (Figure 4.5a) and cross-sectional (Figure 4.5b) SEMs for further growth using $\lambda_1 = 955$ nm to $t_1 = 3.50$ min of the structures first grown using $\lambda_0 = 727$ nm (Figure 4.4). Continued film evolution was observed in a similar manner to that described previously (Figure 4.4), and a period of 370 ± 6 nm was measured at $t_1 = 3.50$ min, quantitatively matching that measured for Λ_{955}.

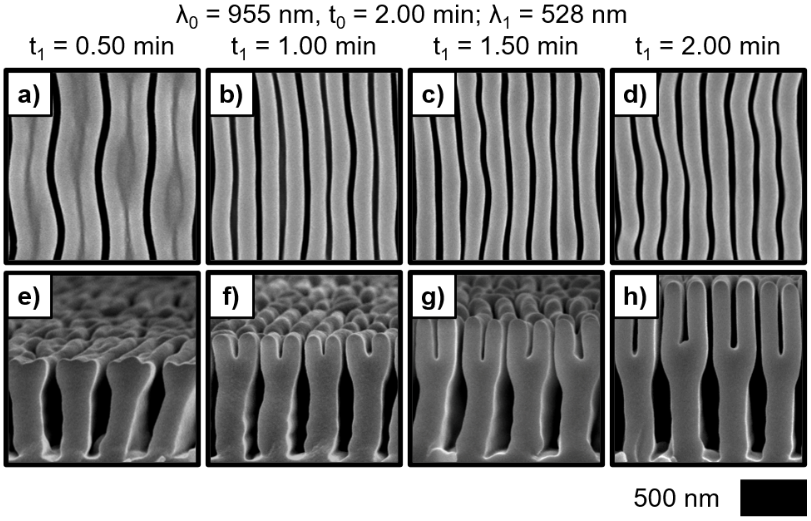

Figure 4.6 (a) – (d) Representative top-down and (e) – (h) cross-sectional SEMs of deposits generated initially using λ_0 = 955 nm for t_0 = 2.00 min, and then extended in a subsequent deposition step using λ_1 = 528 nm for the indicated t_1.

Figure 4.6 presents representative top-down (Figure 4.6a–d) and cross-sectional (Figure 4.6e–h) SEMs of Λ_{955} films that were extended in a second deposition step using λ_1 = 528 nm illumination for the indicated t_1. Initial growth with λ_1 produced sets of three parallel bands consisting of two bright bands with single a darker band in between each pair of bright bands (Figure 4.6a), suggestive of the formation of two new features on top of each preexisting lamella. 2D FT analysis revealed a period of 372 ± 6 nm at t_0 = 0.50 min, corresponding to the larger features defined by λ_0 (955 nm). The periodicity of the smaller nascent features was 189 ± 6 nm, as measured by additional 2D FT analysis of the same SEM data but with contrast thresholding applied. Upon additional deposition using λ_1 = 528 nm, the 189 ± 6 nm morphological period became dominant (Figure 4.6b,c). For t_1 = 1.00 min, the interfacial morphology appeared similar to that observed for growth at Λ_{528} (Figure 4.1a), with a single morphological period of 189 ± 6 nm. Cross-sectional SEM analysis revealed the initial generation of two small features that projected outward from each larger underlying feature (Figure 4.6e), and these features then grew along the substrate normal axis as additional mass was deposited (Figure 4.6f–h). The interfacial period increased from 190 ± 6 nm at $t_1 = 1.50$ min to 197 ± 6 nm at $t_1 = 2.00$.

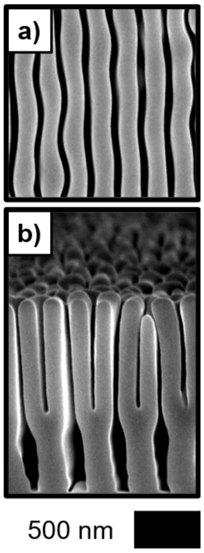

Figure 4.7 (a) Representative top-down and (b) cross-sectional SEMs of deposits generated initially using $\lambda_0 = 955$ nm for $t_0 = 2.00$ min, and then extended using $\lambda_1 = 528$ nm for $t_1 = 3.00$ min.

Figure 4.7 presents top down (Figure 4.7a) and cross-sectional (Figure 4.7b) SEMs for further growth using $\lambda_1 = 528$ nm to $t_1 = 3.00$ min of structures first grown using $\lambda_0 = 955$ nm (Figure 4.6). The interfacial period was observed to increase to 204 ± 6 nm at $t_1 = 3.00$ min, consistent with that measured for Λ_{528}.

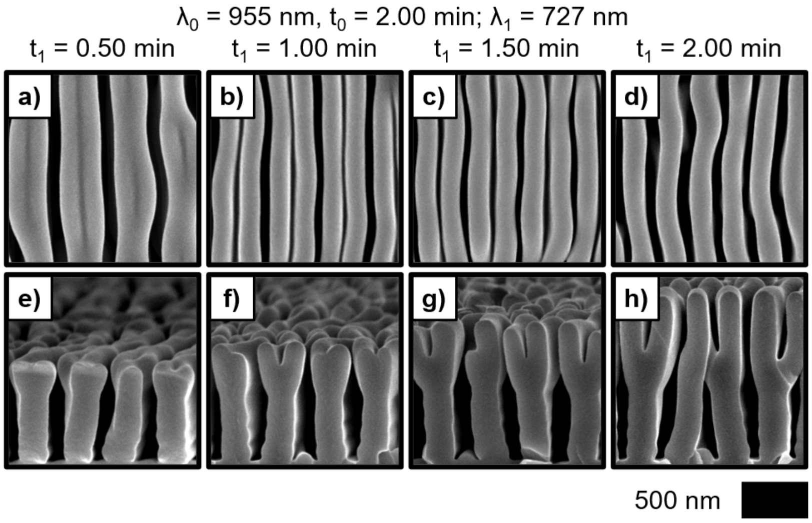

Figure 4.8 (a) – (d) Representative top-down and (e) – (h) cross-sectional SEMs of deposits generated initially using λ_0 = 955 nm for t_0 = 2.00 min, and then extended in a subsequent deposition step using λ_1 = 727 nm for the indicated t_1.

Figure 4.8 presents representative top-down (Figure 4.8a–d) and cross-sectional (Figure 4.8e–h) SEMs of Λ_{955} films extended in a second deposition step using λ_1 = 727 nm illumination for the indicated t_1. At t_1 = 0.50 min, an increase in the interfacial width of the features was observed relative to Λ_{955} (Figure 4.1c). A dark band was also observed along the lamellar centerlines with two brighter regions on either side, indicative of two nascent features on top of each preexisting feature (Figure 4.8a,e), similar to the behavior observed for extended growth of Λ_{955} films using λ_1 = 528 nm (Figure 4.6). Deposition using λ_1 = 727 nm for t_1 = 1.00 min effected further definition of the smaller nascent features, resulting in ordered pairs of lamellae (Figure 4.8b) with widths more similar to those observed for Λ_{727} (Figure 4.1b) than Λ_{955} (Figure 4.1c). At this stage 2D FT analysis revealed two morphological periods, one at 220 ± 8 nm corresponding to the individual features at the interface, and another at 383 ± 8 nm corresponding to the pairs of features. Additional deposition with λ_1 resulted in a loss of pairwise order and a decrease in the density of the individual lamellae (Figure 4.8c,d). A single morphological period of 254 ± 8 nm was measured for $t_1 = 1.50$ min, and this value increased to 272 ± 14 nm at $t_1 = 2.00$ min, in accord with that observed for Λ_{727} (Figure 4.1b). Cross-sectional analysis revealed that two new features were initially generated atop most of the preexisting lamellae, although some preexisting features primarily exhibited an increase in width (Figure 4.8e,f). Upon additional deposition, some features continued to grow linearly along the substrate normal, but others terminated and some exhibited transient growth away from the substrate normal and subsequently fused with a neighboring feature (Figure 4.8g,h).

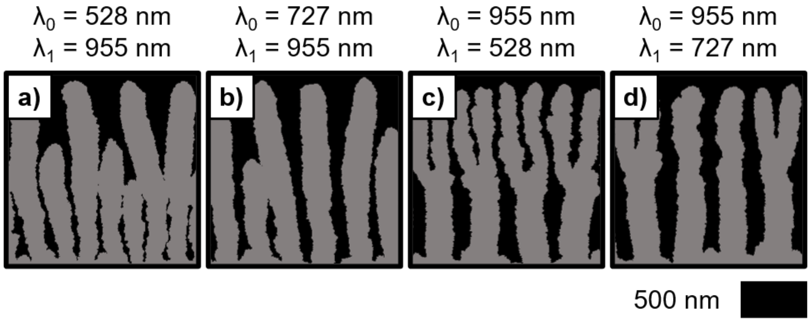

Figure 4.9 Simulated deposit morphologies generated first using the indicated λ_0 illumination and then extended using the indicated λ_1 illumination.

The film growth by light-mediated electrodeposition was simulated using an optically-based, two-step iterative modeling approach. Full-wave electromagnetic simulations were first performed to calculate the spatially resolved magnitude of the light absorption. Mass was then added using a Monte Carlo method in which the local probability of addition was weighted by the previously calculated local absorption. These steps were then successively iterated. Empirical inputs to the model were limited to estimates of the complex refractive index of the deposited Se-Te material and the refractive index of the electrolyte. Figure 4.9 presents simulated film morphologies generated by first modeling the initial deposition using the indicated λ_0 and then modeling extended growth with the indicated λ_1. The pairs of λ_0 and λ_1 values used in the modeling were equivalent to those investigated experimentally (Figure 4.3 – Figure 4.8). The simulated film morphologies closely matched the analogous experimental data (Figure 4.3h, Figure 4.4h, Figure 4.6h, Figure 4.8h), with periodic lamellar features generated in each case and the feature pitch varying along the substrate normal. The interfacial period increased for cases in which $\lambda_1 > \lambda_0$ (Figure 4.9a,b) and decreased for $\lambda_1 < \lambda_0$ (Figure 4.9c,d).

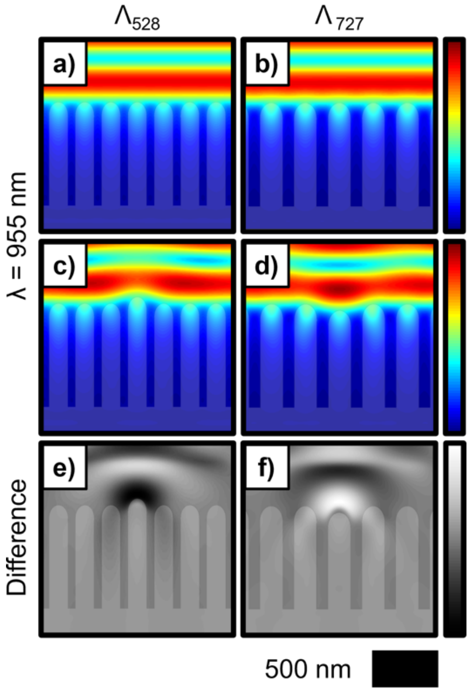

Figure 4.10 (a) and (b) Simulated spatial profiles of the time-averaged E-field magnitude resulting from λ = 955 nm illumination of simplified structures representative of the indicated experimentally observed structures. (c) and (d) same as (a) and (b), respectively, but with the height of a single feature adjusted to model initial extension using λ_1. (e) and (f) Difference between the profiles presented in (a) and (c), and (b) and (d), respectively.

A series of electromagnetic simulations using simplified morphologies was performed to gain insight into the optical phenomena associated with growth using sequential wavelength inputs. Uniform, idealized lamellar structures were designed with dimensions derived from the experimental data. Figure 4.10a,b presents spatial profiles of the time-averaged E-field magnitude for illumination with λ = 955 nm of simulated structures representative of Λ_{528}, and Λ_{727}, respectively. In both cases, the profile was isotropic in the direction of feature periodicity above the growth interface. Spatially isotropic resonances were observed within each feature and were equivalent amongst all observed features. An additional set of simulations was performed in which the idealized structures were modified to include some height anisotropy, in analogy to the experimentally observed morphology evolution following a change in the optical input wavelength from λ_0 to λ_1, wherein $\lambda_1 > \lambda_0$ (Figure 4.3 and Figure 4.4). Figure 4.10c,d presents data analogous to that in Figure 4.10a,b but for structures modified to include a single taller (Figure 4.10c) or shorter (Figure 4.10d) feature. Figure 4.10e presents the difference between the spatial profiles of E-field magnitude depicted in Figure 4.10a and Figure 4.10c, highlighting the effects of the feature height modification. The E-field magnitude increased within the taller feature and decreased within and above the features immediately adjacent to the taller structure. Figure 4.10f presents the difference in the spatial profiles of E-field magnitude depicted in Figure 4.10b and Figure 4.10d. An arc of increased field magnitude was observed above and surrounding the shorter feature and intersecting the neighboring features. Beyond this arc, another arc of decreased field magnitude was observed, with edges that were not localized to a single feature but instead occurred between the first and second nearest neighbors relative to the central feature. The nearest neighbor features were consequently presented with an increased field magnitude on the side nearer to the shorter structure and a decreased field magnitude on the side opposite to the shorter structure.

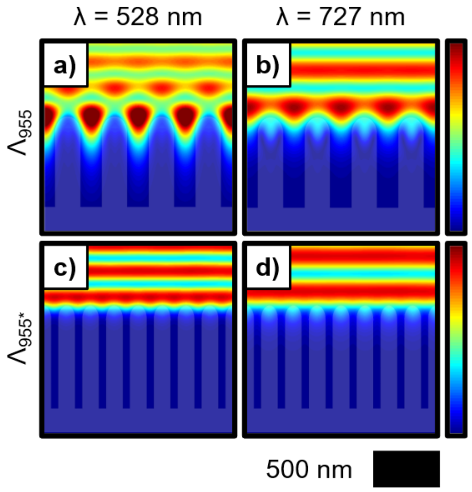

Figure 4.11 (a) and (b) Simulated spatial profiles of the time-averaged E-field magnitude resulting from illumination with the indicated wavelength of simplified structures representative of the experimentally observed Λ_{955} structure. (c) and (d) same as (a) and (b), respectively, but for simplified structures Λ_{955*}, in which the period was half of that measured for Λ_{955}.

Figure 4.11a,b presents spatial profiles of the time-averaged E-field magnitude for illumination of a simplified structure representative of Λ_{955} with $\lambda = 528$ nm, and $\lambda = 727$ nm, respectively. The profiles were mutually similar and exhibited well-defined, intense maxima between the feature tips in addition to local minima directly above each feature. However, for $\lambda = 727$ nm (Figure 4.11b), the maxima between feature tips were less intense and a larger magnitude was observed at the minima above each feature than for $\lambda = 528$ nm (Figure 4.11a). To examine the operative optical processes at a subsequent stage of structural evolution, in which growth with λ_1 approximately doubled the interfacial feature density (Figure 4.6f and Figure 4.8f), simulations were performed using another set of simplified structures. Figure 4.11c,d presents data analogous to that in Figure 4.11a,b, but for structures with a feature pitch that was half that observed for Λ_{955}, denoted as Λ_{955*}. The E-field magnitude resulting from illumination of the Λ_{955*} structure with $\lambda = 528$ nm and $\lambda = 727$ nm was similar, and in both cases the profile was isotropic in the direction of feature periodicity above the growth interface. The correlation between the input wavelength and the morphological period observed for depositions performed using a single illumination input (Figure 4.1) is consistent with the notion that inorganic phototropic growth effects morphological plasticity, analogous to phenotypic plasticity observed in natural systems (as discussed in Chapter 1) in response to static wavelength inputs and spontaneously generates a unique interfacial structure with a discrete period for a discrete value of λ_{avg}.[50] Depositions performed using a single unchanged illumination wavelength effected simple linear extension without a change to the in-plane morphology (Figure 4.2). In contrast, depositions performed using two distinct, sequential illumination inputs wherein $\lambda_1 > \lambda_0$ exhibited termination of some features along the growth axis after the change in input wavelength, in conjunction with a monotonic increase in the interfacial period (Figure 4.3 and Figure 4.4) which eventually matched that observed for deposition using λ_1 alone (Figure 4.1c,f). These results demonstrate a plastic response to a temporally abrupt illumination change in a manner analogous to shade-avoiding plants, which exhibit apical dominance and branching reduction upon encountering far-red illumination.[30,133] Moreover, despite the minimal use of empirical inputs in the modeling, the simulated morphologies (Figure 4.9a,b) closely matched those observed experimentally for extended growth of Λ_{528} and Λ_{727} structures using $\lambda_1 = 955$ nm (Figure 4.3h and Figure 4.4h), suggesting that the structural evolution in response to an increase in the input wavelength is primarily directed by light-material interactions at the growth interface. The operative optical mechanism is illustrated by the associated set of simulations using simplified structures (Figure 4.10). Illumination of simplified Λ_{528} and Λ_{727} structures with $\lambda_1 = 955$ nm indicated no notable anisotropy in the spatial profile of the E-field magnitude (Figure 4.10a,b). This result is consistent with the relatively small feature size and period relative to the input wavelength ($\lambda_1 = 955$ nm) and the lower material absorption coefficient at 955 nm relative to shorter wavelengths, which limits scattering and coupling. These results are suggestive of continued linear extension of all preexisting features. However, stochastic variations in the growth rate of individual features may result in transitory structural anisotropy at the interface. In the case of resonant illumination, ordered growth that maintains isotropic feature sizes is a consequence of cooperative light scattering amongst neighboring features promoting synergistic light absorption.[53] Here, the mismatch between the illumination wavelength ($\lambda_1 = 955$ nm) and the structure (Λ_{528} and Λ_{727}) can effect scattering that enables positive reinforcement, rather than suppression, of transitory anisotropy, and consequently results in structural evolution. The profiles of E-field magnitude for simplified Λ_{528} and Λ_{727} structures including a feature with modified height illuminated with $\lambda_1 = 955$ nm (Figure 4.10c,d) are consistent with this conceptual framework. When height asymmetry was present between neighboring features, the tips of taller features exhibited increased E-field magnitude relative to the isotropic case (Figure 4.10a,b), whereas the tips of shorter features exhibited decreased E-field magnitude. This observation is consistent with the experimental results in which taller features exhibited extended growth, but the growth of shorter features was terminated. In this regard, the characteristics of inorganic phototropic growth resemble the asymmetric competition behavior exhibited by plants in which larger individuals often obtain a disproportionate share of contested resources and suppress the growth of smaller neighbors.[134,135] Additionally, it is of note that the increase in interfacial magnitude at the taller features in the Λ_{727} case was asymmetric, with a larger increase at the side neighboring the shorter feature. This is consistent with the transient off-normal growth of nearest neighbor features towards a terminating feature observed in the experimental data (Figure 4.4). These results arise because the Λ_{727} structure period is not close to an integral fraction of that of the Λ_{955} structure, unlike Λ_{528}, and thus scattering of the illumination results in maximal E-field modulation between, rather than an at, preexisting features.

Depositions performed using two distinct, sequential illumination inputs wherein $\lambda_1 < \lambda_0$ (Figure 4.6 and Figure 4.8) exhibited a progressive evolution of the interfacial feature periodicity after the input change. Moreover, the period decreased as the growth continued and eventually matched that observed for structures generated by growth solely using λ_1 excitation (Figure 4.1a,b,d,e). This process was characterized by a branching phenomenon in which individual preexisting features split along the long in-plane axis, parallel to the input polarization, resulting in pairs of smaller features at the interface that then were subject to further evolution and growth. This result provides an additional demonstration of morphological plasticity in response to an abrupt wavelength input change, and moreover is analogous to the response exhibited by shade-intolerant plants, which, upon encountering shorter wavelength light after exposure to far-red illumination, initiate branching and laterally increase the density of light-gathering organs.[133,136] The simulated morphologies for Λ_{955} structures extended using λ_1 = 528 nm or 727 nm illumination (Figure 4.9c,d) closely resembled those generated experimentally (Figure 4.6h and Figure 4.8h), indicating optical control of the growth evolution as noted previously for the case of multistep growth using $\lambda_1 > \lambda_0$. The operative optical mechanism is again demonstrated by the associated set of simulations using simplified structures (Figure 4.11). Illumination of simplified Λ_{955} structures with λ_1 = 528 nm or 727 nm revealed strong maxima in the E-field near the growth interface in the regions between feature tips which can direct branching growth. This is consistent with the empirical data wherein branching of most preexisting features to generate two new features each is observed (Figure 4.6a,e and Figure 4.8a,e). FT analysis indicated that this process initially decreased the experimentally observed interfacial feature periodicity rapidly to a value lower not only than that observed for Λ_{955}, but also lower than that for structures generated with the respective λ_1 input alone (Λ_{528} or Λ_{727}). Additional growth using λ_1 = 528 nm or 727 nm then effected a gradual increase in the period until it was in accord with that for Λ_{528} or Λ_{727}, respectively. This later increase in the period was associated with the termination of individual features in a manner analogous to that observed for deposition using sequential inputs wherein $\lambda_1 > \lambda_0$. Mechanistically, the similarity between these processes is illustrated by the simulations using a simplified structure, Λ_{955^*}, designed with half the feature period of Λ_{955}, to model pairwise splitting. For illumination with both λ_1 = 528 nm and λ_1 = 727 nm (Figure 4.11c,d), the E-field magnitude showed little spatial anisotropy, reflective of the results observed for illumination of idealized Λ_{528} and Λ_{727} structures with λ_1 = 955 nm (Figure 4.10a,b). This termination process was more qualitatively apparent for λ_1 = 727 nm relative to λ_1 = 528 nm, as in the latter case there was a smaller dimensional mismatch between the structure generated by pairwise branching of the Λ_{955} structure and the Λ_{528} structure, relative to that with the Λ_{727} structure.

For the full the series of input pairs (λ_0, λ_1) explored herein, the two-step deposition process using sequential illumination inputs with $\lambda_0 \neq \lambda_1$ exhibited morphological plasticity and generated an interfacial structure in accord with that observed for growth solely using λ_1. Thus, the interfacial structure at the end of the process was defined only by λ_1: the plastic nature of the response did not depend critically on λ_0 nor on the morphology of the previously defined structure. This is consistent with the E-field anisotropies demonstrated in the simulations using simplified model structures, and suggests that the morphologies defined by λ_0 cannot effectively couple with and accommodate the utilized λ_1 illumination. Rather, the observations indicate an emergent nanophotonic behavior that directs the structural evolution to generate a feature pitch proportional to λ_1.[50,53] The cumulative responsive morphological plasticity of structures evolving via inorganic phototropic growth (Figure 4.3 – Figure 4.8) to changes in λ, wherein each new input is physically recorded, indicates that appropriate manipulation of the temporal illumination can generate mesostructures with tailored complexity in three-dimensions in a continuous growth process. Such structures may be useful in a variety of photonic, fluidic, and electrochemical applications.[131,132,137]

4.3 Conclusions

Se-Te films generated by light-mediated electrodeposition using linearly-polarized illumination from a single narrowband LED source generated ordered, anisotropic mesostructures with nanoscale lamellar features that projected along the substrate normal and morphological periods that were proportional to the input wavelength. Deposits initially generated using a single wavelength input, λ_0, and extended in a subsequent deposition step with a discrete input, λ_1, produced a spontaneous plastic response that eventually resulted in an interfacial morphology matching that observed for deposits generated using λ_1 alone. This structural evolution involved feature termination, branching, and fusion along the growth direction. Such evolution demonstrates the generation of complex morphologies in three-dimensions using a single, continuous growth process via temporal manipulation of the input illumination characteristics. Simulated deposit morphologies generated using a fully optically-based model closely reproduced the morphologies observed experimentally for multistep growth with sequential wavelength inputs, indicating that the plastic response was directed by photonic phenomena at the growth interface. For the cases investigated, deposition using sequential inputs wherein $\lambda_0 < \lambda_1$ exhibited structural evolution primarily via feature termination. Optical simulations using simplified model structures suggested that this plastic response was directed by interfacial scattering that reinforced stochastically generated non-uniformity in the height of the features. In contrast, explored cases of deposition using sequential inputs wherein $\lambda_1 > \lambda_0$ initially exhibited pairwise branching of features, decreasing the feature period to values lower than those observed for structures generated using either λ_0 or λ_1 alone. Further evolution proceeded via feature termination and/or merging of adjacent features. Additional simulations with simplified structures indicated that the initial branching was directed by effective scattering of the shorter λ_1 illumination which produced strong field localization between preexisting features, and then subsequent feature density reduction followed a process analogous to that observed for evolution using sequential inputs with $\lambda_0 < \lambda_1$. The cumulative data thus illustrate the capability of inorganic phototropic growth to exhibit morphological plasticity and to adapt to new wavelength inputs via optical self-regulation, and demonstrates that structures with complexity in three-dimensions can be generated by straightforward manipulation of the optical input characteristics.

Chapter 5

PATH-DEPENDENT MORPHOLOGICAL EVOLUTION OF SE-TE MESOSTRUCTURES PREPARED BY INORGANIC PHOTOTROPIC GROWTH

Adapted with permission from: Hamann, K. R.; Carim, A. I.; Meier, M. C.; Lewis, N. S. Path-Dependent Morphological Evolution of Se–Te Mesostructures Prepared by Inorganic Phototropic Growth. *J. Am. Chem. Soc.* **2020**, *142*, 19840–19843. DOI: 10.1021/jacs.0c09798. Copyright 2020 American Chemical Society.

5.1 Introduction

This chapter expands on the investigations of morphological evolutions in response to changes in illumination wavelength during inorganic phototropic growth described in the previous chapter. A path-dependent "history" effect is described here wherein the film morphology generated in the second step of a two-step inorganic phototropic growth process depends on the preexisting structure that was first grown under different optical stimulation conditions. Growth using first a short wavelength of light, followed by a growth using a longer wavelength, resulted in the second-stage morphology exhibiting termination of lamellae formed during the first growth step. The lamellar pitch at the end of the second growth step was larger than that effected in the first step. In contrast, use of the same input wavelengths but in the opposite order produced no change in the feature pitch but rather only linear feature extension. Analysis of light absorption in the simulated structures, in tandem with the empirical data, indicated that the history effect and asymmetric path dependence resulted from emergent nanophotonic processes at the growth interface that dynamically shaped the optical field and directed interfacial morphological evolution of the deposit in a continuous feedback loop.

5.2 Results and Discussion

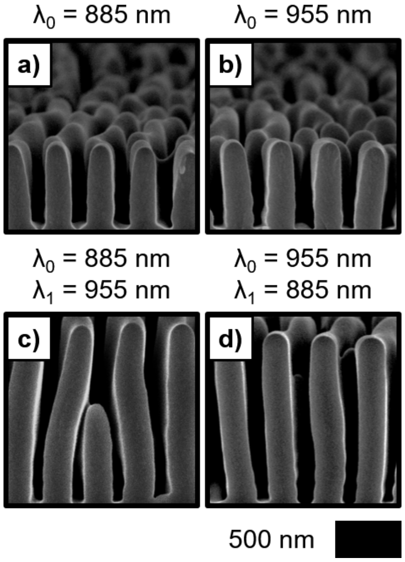

Figure 5.1 Representative cross-sectional SEMs of deposits generated with the indicated λ_0 illumination (a) and (b) and then extended with the indicated λ_1 illumination (c) and (d).

Se-Te was photoelectrochemically grown from an acidic, aqueous solution of oxide precursors. Figure 5.1a,b present representative cross-sectional SEMs of deposits generated using linearly polarized and spatially uniform illumination from LED sources with λ_{avg} of 885 nm or 955 nm. Both deposits exhibited periodic, nanoscale lamellar features that projected outward from the substrate surface along the normal axis, with a high degree of out-of-plane anisotropy. The feature width and pitch effected using λ_{avg} = 955 nm (Figure 5.1b) was greater than that for λ_{avg} = 885 nm (Figure 5.1a). 2D FT analysis of complementary top-down SEM data indicated that the morphological periods of the deposits were 332 ± 2 nm and 363 ± 2 nm for growths with λ_{avg} = 885 nm and 955 nm, respectively. Figure 5.1c presents a representative cross-sectional SEM of a deposit initially grown using $\lambda_{avg} = \lambda_0 =$ 885 nm illumination and then extended using $\lambda_{avg} = \lambda_1 =$ 955 nm. This deposit exhibited a decrease along the substrate normal of the in-plane feature density, with a portion of features exhibiting a termination of growth. Features adjacent to such terminated growth sites were not spatially aligned solely along the surface normal, and some bent towards terminated features. Consequently, the interfacial feature pitch increased to 358 ± 10 nm, in accord with that observed for deposits that were generated using only λ_{avg} = 955 nm (Figure 5.1b). This behavior is consistent with prior results which indicate that each growth wavelength λ_{avg}, by itself produces a single, characteristic lamellar growth period in the resulting film.[50] In contrast, Figure 5.1d presents a representative SEM of a deposit grown in a similar two-step manner as that presented in Figure 5.1c, but with the order reversed such that λ_0 = 955 nm and λ_1 = 885 nm. The features increased in height during the second growth stage, but the resulting morphology was qualitatively similar to growth using only λ_{avg} = 955 nm (Figure 5.1b). No change in the in-plane feature density along the substrate normal was observed, and the interfacial period of 365 ± 2 nm quantitatively matched that observed for growth using only λ_{avg} = 955 nm. The growth was thus clearly path-dependent and asymmetrically exhibited a history effect, with increases in the growth wavelength from 885 nm to 955 nm producing a change in feature density whereas no change was observed when the growth wavelength was instead decreased from 955 nm to 885 nm.

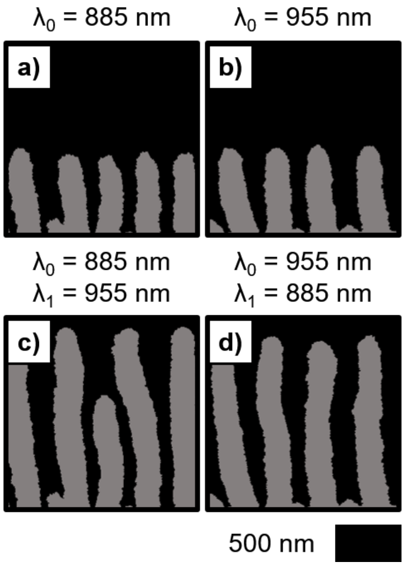

Figure 5.2 Simulated deposit morphologies generated with the indicated λ_0 illumination (a) and (b) and then extended with the indicated λ_1 illumination (c) and (d).

To gain insight into whether the path-dependent growth is an intrinsic consequence of asymmetric evolution of internal optical fields in the emerging, growing deposit, or potentially indicates a structural or chemical metastability, optically-based computer simulations of the growth were performed. A two-step iterative model was utilized wherein electromagnetic simulations of light absorption were used to direct mass addition via a Monte Carlo method. Empirical inputs were limited to estimates of the complex refractive index of the deposits and the electrolyte refractive index. The model contained only Maxwell's equations, with no chemical or structural bias towards selective morphology growth. Figure 5.2 shows that the simulated morphologies generated using optical inputs analogous to those used experimentally (Figure 5.1) closely reproduced the empirical data, including the path-dependent response to the stepped wavelength growth process. The agreement between the experimental and simulation data confirms that the physical origin of the asymmetry in the growth process is ascribable to light-material interactions during growth.

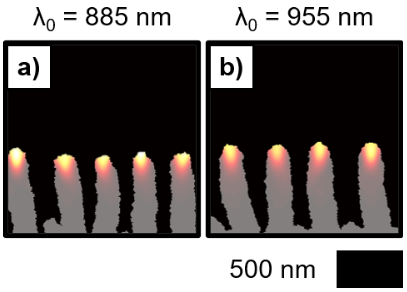

Figure 5.3 Simulated profiles of absorption of the indicated λ_0 illumination in deposit morphologies generated by growth modeling with the same λ_0.

Figure 5.3a and Figure 5.3b present simulated profiles of light absorption in deposit morphologies generated via modeling using λ_{avg} = 885 nm and 955 nm, respectively, and illuminated with the same λ_{avg}. Both profiles exhibited concentrated absorption in the feature tips near the growth interface. Local enhancements in optical absorption result in local increases in mass deposition, so the simulated absorption concentration indicates that material addition should occur preferentially at the feature tips, resulting in linear feature extension. This modeled behavior is consistent with the morphological anisotropy and periodicity observed experimentally and indicates that growth can spontaneously produce a structure that optimizes interfacial optical concentration of the specific light input.

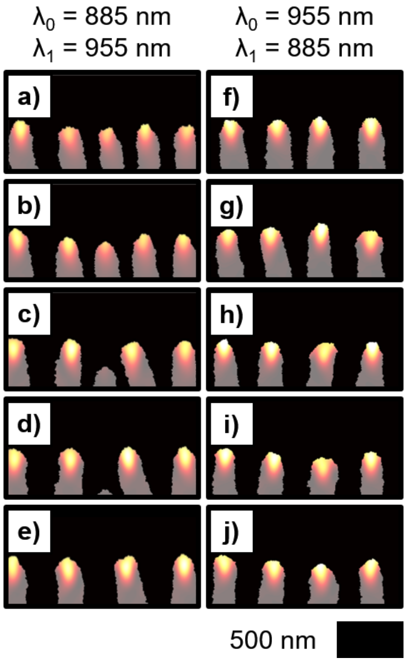

Figure 5.4 Simulated profiles of absorption of the indicated λ_1 illumination in deposit morphologies generated by growth modeling. In each column, panels from top to bottom present profiles for successive iterations of simulated morphologies generated initially using the indicated λ_0 illumination and progressively extended with the indicated λ_1 illumination.

Figure 5.4a–e presents successive simulated profiles of absorption of $\lambda_{avg} = \lambda_1 = 955$ nm during growth after initial structure generation using $\lambda_0 = 885$ (as in Figure 5.2c). First, a similar magnitude and concentration of absorption was present in all lamellar tips (Figure 5.4a), however, the centermost feature exhibited slightly decreased absorption and height relative to adjacent features (Figure 5.4b). The localized decrease in absorption resulted in local attenuation of growth, and thus the centermost feature grew less rapidly than adjacent features (Figure 5.4c). The decreased height resulted a self-reinforcing decrease in local absorption, with concomitant increased absorption in adjacent features and anisotropic localization of the absorption resonances in the tips of the adjacent features collectively stunting growth of the attenuated centermost feature. The asymmetric absorption also directed adjacent features to grow at an inclination from the substrate normal, towards the attenuated feature (Figure 5.4d). The resulting morphological evolution further reduced the absorption in the centermost feature, leading to termination and an increased interfacial feature pitch (Figure 5.4e). At this point in the morphological evolution, the resonances in the nearest neighbor features were localized more symmetrically in the tips, indicating continued linear extension of growth but with the new morphological period. The absorption behavior suggests that the growth process can evolve a deposit along the out-of-plane dimension to optimize the interfacial optical concentration in response to a change in input λ_{avg}. This evolution is a consequence of positive feedback, wherein regions coupling more effectively with the new optical input exhibit elevated rates of growth and increased light harvesting, as well as of negative feedback, wherein regions not coupling effectively exhibit decreased rates of growth, lessening parasitic absorption.

Figure 5.4f–j presents similar profiles of light absorption as in Figure 5.4a–e, but for absorption of $\lambda_{avg} = \lambda_1 = 885$ nm after initial growth using $\lambda_0 = 955$ nm (i.e. Figure 5.2d). Initially, all lamellar tips exhibited nearly identical magnitudes and degrees of concentration of optical absorption (Figure 5.4f). In each of the subsequent simulations (Figure 5.4g–j) the absorption intensity in certain features increased, but then regressed again in later simulations, and the opposite behavior was also observed. Simultaneously, in certain iterations the locations of specific absorption resonances deviated from the center of the feature tips, which led to transient growth at an inclination from the substrate normal. However, in later simulations the absorption concentration shifted to the opposite side of the same features, reversing the inclination and thereby resulting in net progressive growth normal to the substrate. These temporal oscillations in the absorption, both in magnitude and in spatial location, indicate that dynamic linear extension of the interfacial morphology defined by the initial optical input (λ_0) can sufficiently accommodate coupling with the new optical input (λ_1) in a manner that suppresses a change in the interfacial feature density and mesoscale structural evolution. The path-dependent asymmetry in the morphological evolution in response to equal magnitude changes in the optical input (λ_{avg}) observed here is thus ascribable to the capacity of the initial structure, defined by λ_0 = 955 nm, to evolve linearly in response to λ_1 = 885 nm, with the greater feature width and pitch enabling dynamic accommodation of coupling to the shorter wavelength through oscillation of the absorption resonances. The finding that the path dependence observed experimentally also spontaneously emerged from the optical growth modeling, which utilized only optical constants and Maxwell's equations, provides strong support for the conclusion that the path-dependent structures do not represent chemically or kinetically metastable states nor reflect specific chemical or structural interactions. The observed behavior is instead a direct consequence of the interplay between light and matter that underpins inorganic phototropic growth: a dynamic, synergistic feedback loop wherein the growing material shapes the near-field optical profile, promoting and focusing subsequent mass deposition and thus responsively shaping the growing material.

5.3 Conclusions

In summary, a history effect was observed during inorganic phototropic growth wherein an initial mesostructure, defined by an initial input wavelength, influenced subsequent growth with a second, distinct input wavelength, to produce a different morphology in the second phase of growth than was produced via single-stage growth with this second input wavelength as the only input. This effect exhibited an asymmetric path dependence wherein discrete mesoscale structural evolution could be directed by the use of two sequential, discrete wavelength inputs, yet the use of the same inputs, but in the opposite order, resulted in only linear extension of the initial growth features. The collective data showed that this path-dependent history effect is a result of the emergent nanophotonic phenomena directing light absorption dynamically during growth as opposed to a chemical or crystallographic disposition. Dynamic, metastable accommodation of a new optical input during growth suppressed mesostructural evolution.

Chapter 6

EMERGENT GENERATION OF MESOSTRUCTURES WITH DUAL, ORTHOGONAL INTERFACIAL PERIODICITIES VIA INORGANIC PHOTOTROPIC GROWTH

Hamann, K. R.; Carim, A. I.; Meier, M. C.; Lewis, N. S. Emergent Generation of Mesostructures with Dual, Orthogonal Interfacial Periodicities via Inorganic Phototropic Growth. *In Preparation.*

6.1 Introduction

Inorganic phototropic growth has been used to generate highly ordered mesostructured morphologies in a variety of materials. Linearly polarized illumination can effect generation of highly ordered, anisotropic, and periodic lamellar structures wherein the direction of periodicity is perpendicular to the direction of the E-field vector of the input illumination, as has been shown in preceding chapters. In this chapter, inorganic phototropic growth of Se-Te was effected using linearly polarized illumination with a series of static, single, short (green to ultraviolet) input wavelengths. The resulting mesostructures exhibited periodic ordering in two orthogonal directions: both perpendicular but also, surprisingly, parallel to, the E-field vector of the input illumination. A growth time series was used to examine structural evolution in both in-plane directions. Optically-based growth modeling was performed to first confirm the optical basis for structural evolution, and then examine the nanophotonic behavior that instructed the generation of the bidirectional, orthogonally periodic mesostructures observed experimentally.

6.2 Results and Discussion

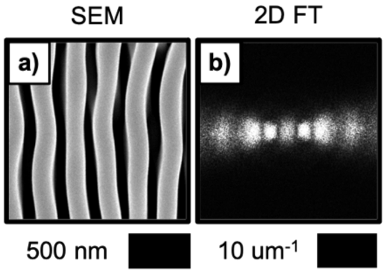

Figure 6.1 (a) Top-down SEM of Se-Te films generated via inorganic phototropic growth using vertically polarized illumination with λ_{avg} = 727 nm. (b) 2D FT calculated from SEM data similar to that presented in (a).

Inorganic phototropic growth of Se-Te films was effected via light-mediated electrochemical deposition from aqueous solution using low-power LED sources polarized linearly with the E-field vector oriented along the vertical. Figure 6.1a presents a representative top-down SEM of a film generated using illumination with λ_{avg} of 727 nm for t = 2.00 min. The film exhibited highly anisotropic lamellar features with defined periodicity in the horizontal direction, perpendicular to the input E-field vector. Figure 6.1b presents a 2D FT derived from SEM data analogous to that presented in Figure 6.1a. Intensity in a FT indicates periodicity in the data from which the FT was calculated: the distance from the center indicates the frequency, and the direction to the center indicates the direction of periodicity. Intensity was only observed along the horizontal axis, which indicated morphological periodicity in the films was isolated to that direction. The FT was quantified, and multiple bands of intensity, all related to a single family of harmonics, were observed, which indicated the film was not perfectly described by a single sinusoidal function. Analysis of the first fundamental peak revealed a morphological period of 263 ± 6 nm.

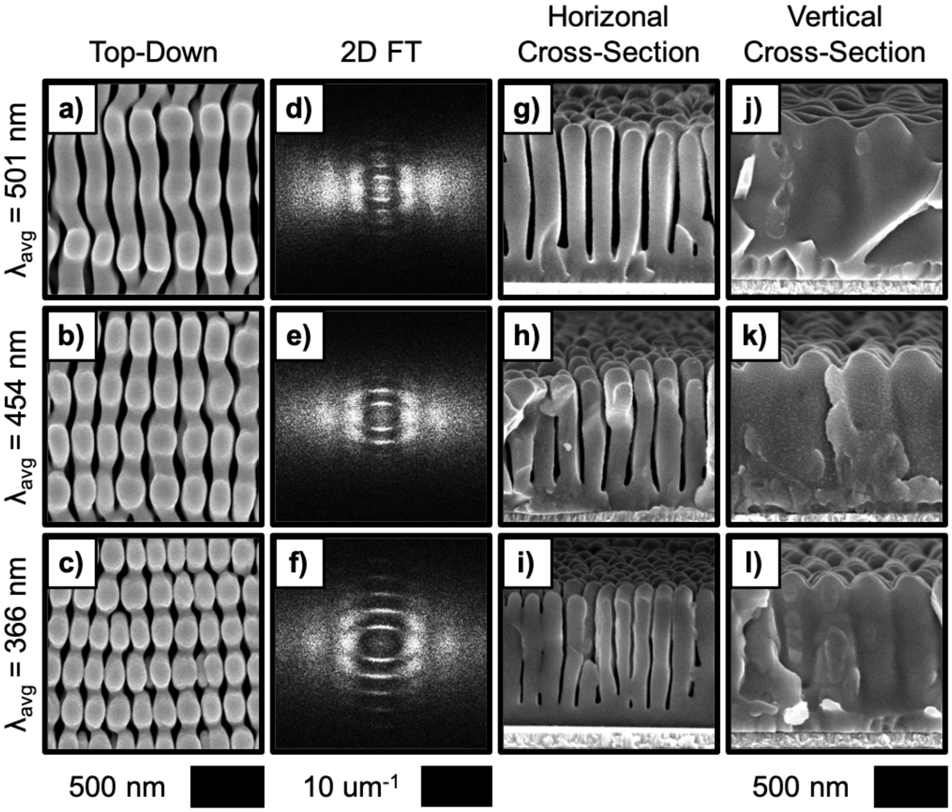

Figure 6.2 (a) – (c) Top-down SEMs of films generated with vertically polarized illumination with the indicated λ_{avg} values. (d) – (f) 2D FTs calculated from SEM data of films shown in (a) – (c). (g) – (l) Cross-sectional SEMs of films shown in (a) – (c), acquired by cleaving samples along the (g) – (i) horizontal and (j) – (l) vertical axes.

Figure 6.2a–c presents top-down SEMs analogous to that presented in Figure 6.1a but for films generated with a series of shorter input λ_{avg} values, as indicated, and Figure 6.2d–f presents related 2D FT data. Growth using λ_{avg} = 501 nm (Figure 6.2a) effected lamellar morphologies similar to those observed for growth using λ_{avg} = 727 nm (Figure 6.1a), but with a smaller feature pitch and, notably, periodic nodules along the tops of the lamellar interfaces. The associated 2D FT data exhibited bands of intensity in both the horizontal and vertical directions, and the sets of bands in both the horizontal and the vertical were observed to each be comprised of a family of related harmonics (Figure 6.2d). Analysis of the position of the first fundamental in the horizontal and vertical directions revealed morphological periods of 206 ± 10 nm and 409 ± 6 nm, respectively. Growth using λ_{avg} = 454 nm resulted in a morphology similar to that observed for growth using λ_{avg} = 501 nm (Figure 6.2a), but with more consistent and well-defined nodules that were smaller and more closely spaced (Figure 6.2b). 2D FT analysis of the film presented in Figure 6.2b revealed periods of 190 ± 6 nm and 353 ± 6 nm along the horizontal and vertical directions, respectively (Figure 6.2e). Growth using λ_{avg} = 366 nm effected a mesostructured interface which had a densely packed two-dimensional square array of nodules which appeared to be aligned and periodic in both the vertical and horizontal dimensions, and some underlying lamellar structure was observed in the spaces between vertically neighboring nodules (Figure 6.2c). 2D FT analysis of the film presented in Figure 6.2c indicated periods of 158 ± 6 nm and 278 ± 6 nm in the horizontal and vertical directions, respectively (Figure 6.2f). The films presented in Figure 6.2a–c were also analyzed via cross-sectional SEM. Figure 6.2g–i and Figure 6.2j–l present cross-sectional SEMs of films generated with the indicated λ_{avg} illumination conditions, acquired by cleaving samples along the horizontal and vertical axes, respectively. The horizontal cross-section SEMs revealed lamellae with significant out-of-plane anisotropy which projected normal from substrate (Figure 6.2g–i). These data indicate that nodule generation atop the lamellae did not reduce the out-of-plane anisotropy in the direction perpendicular to the polarization axis. The vertical cross-section SEMs presented in Figure 6.2j–l reveal the sidewall morphology of single lamella. These features exhibited a periodic interfacial structure consistent with the observation of nodules in the top down data (Figure 6.2a–c), and an isotropic layer of material near the growth substrate. The interfacial nodules appeared larger in width, had less out-of-plane anisotropy, and were more confined to the interface than the lamellae observed in Figure 6.2g–i.

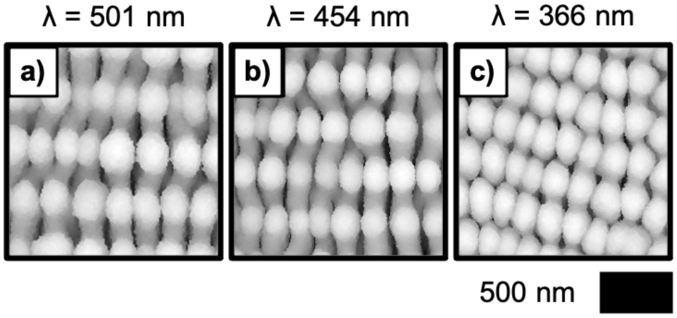

Figure 6.3 Simulated morphologies of films generated via inorganic phototropic growth using vertically polarized illumination with the indicated λ_{avg} values.

An optically-based, two-step iterative growth model was used to simulate inorganic phototropic growth of Se-Te films at short wavelengths. Briefly, absorption was first simulated using full-wave electromagnetic simulations, and then a finite amount of mass was added using a Monte Carlo method, wherein the location of mass addition was probabilistically weighted based on the absorption data calculated in the preceding step; the steps were then iterated to simulate growth. Empirical inputs were limited to the complex refractive index of the Se-Te material and the electrolyte index. Figure 6.3 presents simulated films generated using the indicated simulated illumination conditions. Ordered mesostructured morphologies with periodic components in two orthogonal directions were observed in simulation (Figure 6.3) which closely matched those observed experimentally (Figure 6.2a–c). This agreement between experimental and modeling results, despite limited empirical inputs to the growth simulation, indicates the emperically observed morphologies are principally optically-directed.

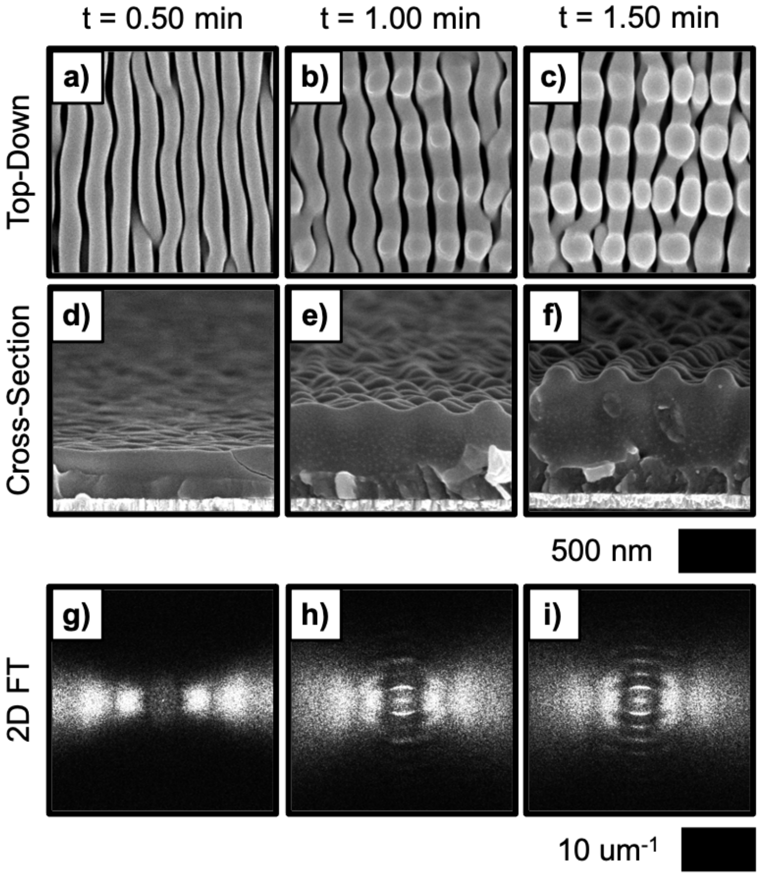

Figure 6.4 (a) – (c) Top-down and (d) – (f) cross-sectional SEMs of films generated using vertically polarized illumination with λ_{avg} = 454 nm for the indicated t. Cross-sections were acquired by cleaving samples along the vertical axes.

To examine the structural evolution during growth, a series of experiments at varied time points was performed. Figure 6.4a–c presents representative top-down SEMs of films generated via inorganic phototropic growth using vertically polarized illumination with λ_{avg} = 454 nm (same as in Figure 6.2b,h,k) for the indicated time. Figure 6.4d–f presents cross-sectional SEMs of films equivalent to those shown in Figure 6.4a–c, acquired by cleaving the samples along the vertical axes, and Figure 6.4g–i presents 2D FT data generated from top-down SEMs similar to those shown in Figure 6.4a–c. At early growth times, anisotropic lamellar structures were observed which appeared periodic in the horizontal direction (Figure 6.4a). The features appeared to have smooth top interfaces and no additional periodic components were observed. Cross-sectional SEM and FT analysis corroborated this observation: the feature height was uniform (Figure 6.4d) and no intensity was observed along the vertical direction of the FT (Figure 6.4g). Upon additional growth, periodic nodules were observed atop some lamellae (Figure 6.4b). The nodules appeared smaller and at a lower density than those observed for an extended growth duration (Figure 6.2b). Cross-sectional analysis (Figure 6.4e) revealed nodule heights which were smaller than those observed for longer growth times (Figure 6.2k) and 2D FT analysis confirmed the presence of an ordered, periodic component in the vertical direction (Figure 6.4h). The nodules appeared to increase in size, density, and height, and became more well-defined, with additional deposition (Figure 6.4c,f). The observed vertical bands in the associated 2D FT were more well-defined and more numerous than the horizontal bands, which indicated increased order in the vertical direction (Figure 6.4i).

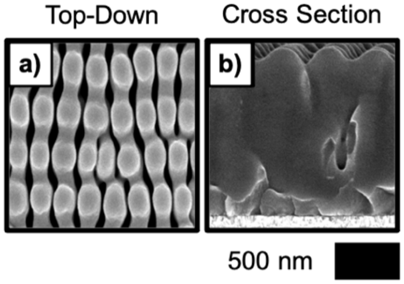

Figure 6.5 (a) Top-down and (b) cross-sectional SEM of films generated using vertically polarized illumination with λ_{avg} = 454 nm for t = 2.50 min.

Figure 6.5 presents top-down (Figure 6.5a) and cross-sectional (Figure 6.5b) SEMs of films generated using λ_{avg} = 454 nm extended to t = 2.50 min. The extended growth duration did not produce further changes to the in-plane size or density of the nodules (Figure 6.5a). The lamellae appeared to continue extension along the out-of-plane direction, but no significant increases in nodule height were observed (Figure 6.5b) relative to those observed at t = 2.00 min (Figure 6.2k). Measurements taken from cross-sectional data revealed average nodule heights of 103 ± 10 nm, 119 ± 12 nm, and 116 ± 12 nm for growths performed for t = 1.50 min (Figure 6.4f), 2.00 min (Figure 6.2k), and 2.50 min (Figure 6.5b), respectively. This suggests that the nodules achieve a steady-state height and do not continue to increase in out-of-plane anisotropy with further mass addition. These data imply that the two orthogonal periodic components arise and evolve separately, and the mismatch in out-of-plane anisotropy between the two sets of orthogonally periodic features suggests the fundamental interfacial light-matter interactions which direct such evolution may be distinct.

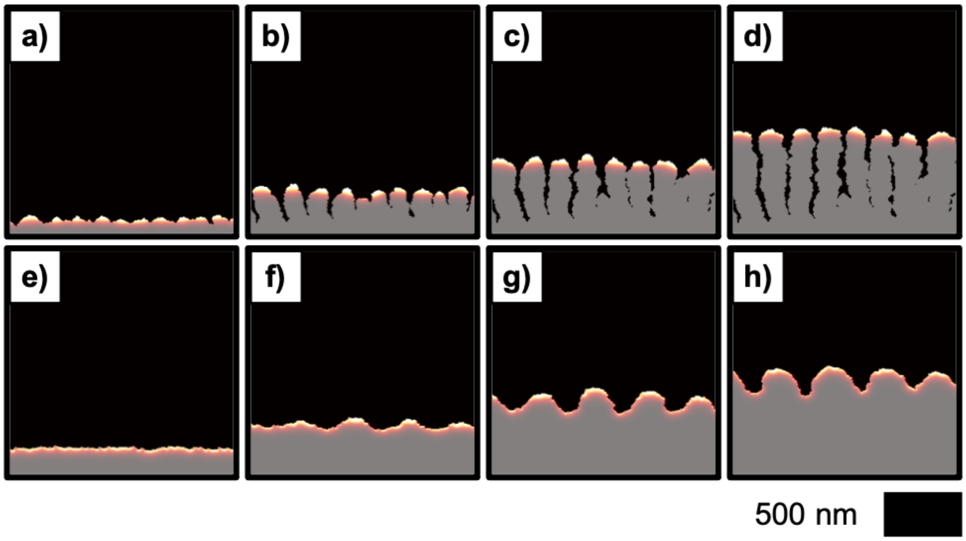

Figure 6.6 Simulated profiles of absorption of $\lambda_{avg} = 454$ nm illumination in morphologies generated by growth modeling with the same illumination wavelength. 2D growth simulations were performed with the polarization axis aligned (a) – (d) perpendicular and (e) – (h) parallel to the simulation plane. In each row, each successive frame represents sequential iterations of simulated growth.

Additional growth simulations were performed to model the development of the orthogonal periodic components. Figure 6.6a–d presents successive profiles of light absorption of $\lambda_{avg} = 454$ nm illumination within structures generated via 2D growth modeling using illumination of the same wavelength. The polarization vector was aligned perpendicular to the simulation plane and thus the simulations represent a cross-sectional view of features similar to that shown in Figure 6.2g–i. In early stages of growth, an oscillatory absorption profile was observed at the interface (Figure 6.6a). Spatially anisotropic absorption effected anisotropic mass addition, and the resulting absorption for all subsequent growth stages was highly concentrated within the tip of each lamellar feature (Figure 6.6b–d). The feedback between spatially concentrated absorption and selective mass addition effected linear, anisotropic feature extension along the out-of-plane direction. Figure

6.6e–h presents similar successive profiles of light absorption as those shown in Figure 6.6a–d, but for simulated growth using λ_{avg} = 454 nm wherein the polarization vector was aligned parallel to the simulation plane; these simulations thus present a cross-sectional view of sidewalls of single lamellae, similar to that shown in Figure 6.2j–l and Figure 6.4d–f. At early stages of growth, light absorption was isotropically confined to the interface (Figure 6.6e). Upon mass addition, some spatial variation in absorption magnitude was observed at the interface (Figure 6.6f). Additional simulated growth preferentially added mass in the regions of highest light absorption and thus effected structured, periodic nodules at the interface (Figure 6.6g). Light absorption magnitude was higher in these nodules, although some absorption magnitude was also observed in the valleys between nodules. Additional simulated growth sustained the structured interfacial nodules but did not increase the out-of-plane anisotropy of these features (Figure 6.6h). The absorption at the nodule tips was observed to fluctuate in magnitude between simulated growth steps, and some absorption magnitude was consistently observed at the valleys between nodules (Figure 6.6g,h). This is distinct from the absorption concentration behavior observed in the orthogonal direction (Figure 6.6a–d) and indicates that optical absorption is not consistently nor sufficiently concentrated within nodule tips to drive anisotropic out-of-plane evolution of the features. This result is consistent with experimental results wherein the nodules do not possess significant out-of-plane anisotropy and, after reaching a certain height, do not continue to increase in height with subsequent mass addition (Figure 6.2j–l, Figure 6.4d–f, Figure 6.5b). These collective light absorption data demonstrate that differences in interfacial optical absorption in each set of orthogonally ordered structures effect distinct out-of-plane growth behavior. For the lamellar features, absorption was highly concentrated within feature tips which instructed localized mass addition at each lamellae tip and thus effected linear and anisotropic feature growth. In contrast, absorption was not highly concentrated within the nodule tips, and some magnitude was consistently observed in the valleys between nodules. Additionally, the absorption magnitude within each nodule was not constant but oscillated in magnitude with mass addition. As a result, the nodules did not increase in out-of-plane anisotropy with further growth, but instead maintained a consistent height at the interface.

6.3 Conclusions

In summary, inorganic phototropic growth of Se-Te films using linearly polarized illumination sources with sufficiently short λ_{avg} values effected the generation of mesostructured morphologies with unique in-plane and out-of-plane anisotropies and distinct periodic ordering in two mutually orthogonal directions, aligned parallel and perpendicular to the polarization source. Optically-based growth modeling successfully reproduced the morphologies observed experimentally. Simulated light absorption data indicated distinct optical concentration within each of the sets of orthogonally ordered features effected the unique anisotropies observed. In one direction, highly concentrated light absorption effected highly anisotropic lamellar features, which continued to increase in out-of-plane height with additional growth. In the other, orthogonal direction, insufficiently concentrated absorption within the tips of the nodules, as well as the presence of absorption magnitude in the area between neighboring nodules, prevented increases in the out-of-plane height of these features and instead isolated them to the interfacial region atop lamellae. These results demonstrate the capability to generate mesostructured films with unique in-plane and out-of-plane anisotropies and periodic ordering in two orthogonal directions in a single growth step using a single, static illumination input.

Chapter 7

METHODS

This chapter details the experimental and computational methods used to generate the data presented in the preceding chapters.

7.1 Materials and Chemicals

H_2SO_4 (ACS Reagent, J. T. Baker), buffered HF improved etchant (Transene), In (99.999 %, Alfa Aesar), Ga (99.999 %, Alfa Aesar), $CdSO_4$ (99+ %, Sigma-Aldrich), $Pb(ClO_4)_2 \cdot 3H_2O$ (99%, Acros Organics), TeO_2 (99+ %, Sigma-Aldrich), and CS_2 (99.9+ %, Alfa Aesar) were used as-received. Chapter 2 and Chapter 3 used SeO_2 (99.999 %, Acros Organics) as-received. Chapter 4, Chapter 5, and Chapter 6 used SeO_2 (99.4 %, Alfa Aesar) as-received. H_2O with a resistivity ≥ 18.2 MΩ cm (Barnstead Nanopure System) was used throughout. Au-coated n^+-Si(100) (< 0.005 Ω cm, As-doped, 525 ± 25 μm, single-side polished, Addison Engineering) was used as a substrate for deposition. Flash-Dry Ag Paint (SPI Supplies), EP21ARHTND Epoxy (MasterBond), and nitrocellulose-based nail polish were used to assemble the working electrodes.

7.2 Substrate Preparation

n^+-Si wafers were etched with buffered HF for 30 s, rinsed with H_2O, dried under a stream of $N_{2(g)}$, and then immediately transferred to an electron-beam metal evaporator with a base pressure < 10^{-5} torr. Using an accelerating voltage of 10 kV, a 10-nm Ti adhesion layer was deposited on the polished side of the wafer using a 50-mA deposition current. For the substrates used in Chapter 2, Chapter 3, and Chapter 6, a 50-nm Pt capping layer was then deposited atop the Ti layer using a 150-mA deposition current. For the substrates used in Chapter 2 and Chapter 3, the wafers were then transferred to a RF sputterer in which a 100-nm Au layer was deposited atop the Pt layer using a RF power of 80 W. For the substrates used in Chapter 4 and Chapter 5, a 50-nm Au layer was deposited atop the Ti layer using a 150-mA deposition current, and then a 20-nm Ti layer was deposited on the unpolished side of the wafer to serve as a back-contact. All metal-topped Si sections were cut into square 0.50 by 0.50 cm sections for use as deposition substrates.

7.3 Electrode Preparation

For the experiments described in Chapter 2 and Chapter 3, electrode bodies were constructed with glass tubing and a wire contact. One end of a Sn-coated Cu wire (22 AWG) was bent to form a small, flat coil and the wire was threaded through glass tubing (6 mm O. D.) such that the coil was just outside the tubing. Epoxy was applied to seal the end of the tube from which the coil protruded. A eutectic mixture of Ga and In was scratched with a carbide-tipped scribe into the unpolished back surfaces of the Au-topped Si sections. The wire coil was then contacted to the unpolished surface and affixed with Ag paint. Nail polish was applied to insulate the unpolished face, the wire-coil contact, and the exposed wire between the coil and epoxy seal. Immediately before deposition, the surface of each electrode was briefly cleaned using a stream of $N_{2(g)}$.

For the experiments described in Chapter 4, Chapter 5, and Chapter 6, electrode bodies were constructed with aluminum half-rounds. Electrode assemblies were prepared by applying epoxy to the flat sides of each of two Al half-round bars (0.25 in diameter). The two bars were then joined together, with a ~ 10 mm offset in the axial dimension to form a cylinder with two half-round ends. Polytetrafluoroethylene heat-shrink tubing was used to insulate the cylindrical section and epoxy was used to insulate the rounded side of one of the half-round ends. For the substrates used in Chapter 4 and Chapter 5, Ag paint was applied to the Ti-coated back surfaces of the Au-topped Si sections and the sections were affixed to the flat surface of the epoxied half-round end. For the substrates used in Chapter 6, a eutectic mixture of Ga and In was scratched with a carbide-tipped scribe into the unpolished back surfaces of the Pt-topped Si sections, and Ag paint was used to affix the sections to the flat surface of the epoxied half-round ends. Nail polish was used to insulate the remaining uncovered area on the flat surface that surrounded the metal-topped Si sections. Immediately before deposition, the surface of each electrode was briefly cleaned using a stream of $N_{2(g)}$.

7.4 Electrode Illumination

Illumination for most of the photoelectrochemical depositions was provided by narrowband diode (LED) sources (Thorlabs) with respective intensity-weighted average wavelength, λ_{avg}, values and spectral bandwidths (FWHM) of 366 nm and 7.5 nm (M365L2), 454 nm and 20 nm (M455L2), 458 nm and 20 nm (SOLIS-460A), 501 nm and 37 nm (M505L4), 528 nm and 32 nm (SOLIS-525B or SOLIS-525C), 626 nm and 17 nm (SOLIS-623C), 727 nm and 37 nm (M730L4), 727 nm and 40 nm (M730L5), 859 nm and 39 nm (SOLIS-850C), and 955 nm and 60 nm (M970L4). The LED with λ_{avg} = 859 nm (SOLIS-850C) was used in conjunction with a long pass filter with an 875-nm cut-on wavelength (Edmund Optics, 64-684) to provide illumination with a λ_{avg} value of 885 nm with a FWHM of 11 nm. Additionally, a broadband LED source (SOLIS-3C) was used in conjunction with a 550-nm bandpass filter (Edmund Optics 33-330) to produce illumination with a λ_{avg} value of 550 nm and a FWHM of 93 nm.

Illumination from the λ_{avg} = 366, 454, 501, 727, and 955 nm sources was collected, condensed, and collimated using a single aspheric lens (Ø50.8 mm, f = 32 mm). For all other LEDs, three lenses in series were utilized: first, an aspheric lens (Ø25.4 mm, f = 16 mm), and second, a bi-convex lens (Ø50.8 mm, f = 60 mm). For the experiments described in Chapter 2, an aspheric lens (Ø30 mm, f = 26 mm) was used as the third element. For the experiments described in Chapter 3, an aspheric lens (Ø50.8 mm, f = 32 mm) was used as the third element. For the experiments described in Chapter 4 and Chapter 5, a bi-convex lens (Ø50.8 mm, f = 100 mm) was used as the third element. For experiments using polarized illumination, a dichroic film polarizer (Thorlabs LPVISE200-A, LPNIRE200-B, or WP25M-UB) was inserted along the beam path. For experiments involving simultaneous illumination with two sources, a polka dot beamsplitter (Thorlabs BPD508-G) was utilized to combine the outputs; both sources were incident upon the beamsplitter at an angle of 45° from the surface normal and thus generated coaxial output. For all experiments, a 1500-grit ground-glass (N-BK7) diffuser was placed immediately in front of the photoelectrochemical cell to ensure spatial homogeneity of the illumination.

The light intensity incident on the electrode was measured by placing a calibrated Si photodiode (Thorlabs FDS100) instead of an electrode assembly in the photoelectrochemical cell with electrolyte, and the steady-state current response of that Si photodiode was measured. Depositions utilizing the diodes with λ_{avg} = 366, 454, 458, 501, 550, 626, 859, and 885 nm were performed with light intensities of 0.025, 0.030, 0.250, 0.030, 0.250, 0.500, 1.500, and 0.110 W cm^{-2}, respectively. Depositions utilizing a single illumination source wherein λ_{avg} = 727 nm were performed with light intensities of 0.056 and 0.050 W cm^{-2} for the experiments described in Chapter 4 and Chapter 6, respectively. Depositions utilizing a single illumination source wherein λ_{avg} = 528 nm were performed with light intensities of 0.500, 0.250, and 0.038 W cm^{-2} for the experiments described in Chapter 2, Chapter 3, and Chapter 4, respectively. Depositions utilizing a single illumination source wherein λ_{avg} = 955 nm were performed with light intensities of 0.130 and 0.123 W cm^{-2}, for the experiments described in Chapter 4 and Chapter 5, respectively. For depositions performed using simultaneous illumination from two orthogonally polarized sources, a total light intensity of I_0 = 0.250 W cm^{-2} was used, wherein an intensity of $0.7 \cdot I_0$ was provided by one source and an intensity of $0.3 \cdot I_0$ was provided by the orthogonally polarized source.

7.5 Photoelectrochemical Deposition

All photoelectrochemical depositions were performed using a Bio-Logic SP-200 potentiostat and a single-compartment glass cell with a quartz window. A three-electrode configuration was utilized with a Ag/AgCl reference electrode (3.00 M KCl, Bioanalytical Systems). For the experiments described in Chapter 2 and Chapter 3, a graphite-rod counter electrode (99.999 %, Sigma-Aldrich) was used. For the experiments described in Chapter 4, Chapter 5, and Chapter 6, an Ir wire counter electrode (99.999 %, Sigma-Aldrich) isolated behind a porous glass frit was used. The metal-coated electrode was illuminated as detailed above in Section 7.4. For the experiments described in Chapter 2, Se-Pb films were deposited from an aqueous solution of 0.0100 M SeO_2, 0.0050 M $Pb(ClO_4)_2$, and 0.100 M $HClO_4$ by biasing the illuminated Au-coated electrode potentiostatically at 0.00 V vs. Ag/AgCl for 10.00 min at room temperature. For the experiments described in Chapter 3, Se-Cd films were deposited from an aqueous solution of 0.00500 M SeO_2, 0.200 M $CdSO_4$, and 0.100 M H_2SO_4 by supplying a current density of j = -0.50 mA cm^{-2} to the illuminated Au-coated electrode at room temperature until a charge of Q = -1.0 C cm^{-2} had passed. For the experiments described in Chapter 4 and Chapter 5, Se-Te films were deposited from an aqueous solution of 0.0200 M SeO_2, 0.0100 M TeO_2, and 2.00 M H_2SO_4 by supplying a current density of j = -8.00 mA cm^{-2} to the illuminated Au-coated electrode for t_0 = 2.00 min (charge density of Q_0 = 0.96 mC cm^{-2}). For depositions using two sequential, discrete illumination inputs, the electrode was transiently floated to open circuit following initial deposition as the illumination input was changed, and then deposition was continued with the new illumination input by supplying -8.00 mA cm^{-2} for an additional t_1 = 0.50 – 2.00 min (additional charge density of Q_1 0.24 – 0.96 mC cm^{-2}), unless otherwise noted. For the experiments described in Chapter 6, Se-Te films were deposited from an aqueous solution of 0.0200 M SeO_2, 0.0100 M TeO_2, and 2.00 M H_2SO_4 by supplying a biasing the Pt-coated electrode potentiostatially at -0.150 V vs. Ag/AgCl for 2.00 min, unless otherwise noted.

After growth, the electrode was immediately removed from the cell, rinsed with H_2O, and then dried under a stream of $N_{2(g)}$. The metal-coated substrate with top-facing photoelectrodeposit was mechanically separated from the rest of the electrode assembly. The nitrocellulose-based insulation and the majority of the Ag paint, and any In-Ga eutectic, were then removed mechanically.

7.6 Deposit Post-Processing

Electrodes supporting a photoelectrodeposited Se-Pb film were removed from the cell, rinsed with H_2O, and then dried under a stream of $N_{2(g)}$. Electrodes were then transferred to a single-compartment glass cell and immersed in 0.500 M H_2SO_4. A three-electrode configuration was utilized with a graphite-rod counter electrode and a saturated calomel reference electrode (SCE, CH Instruments). The electrode was biased potentiostatically at -0.35 V vs. SCE for 5.00 min at room temperature to effect the reductive elimination of Se from the films and thereby produce stoichiometric PbSe.

Electrodes supporting a photoelectrodeposited Se-Cd film were removed from the cell, rinsed with H_2O, and then dried under a stream of $N_{2(g)}$. Electrodes were transferred to a round-bottom glass flask and immersed in $CS_{2(l)}$. The $CS_{2(l)}$ was maintained at the boiling point (46° C) under reflux for 15 h to effect the elimination of excess Se from the films and thereby produce stoichiometric CdSe.

Following electro-/chemical treatment, the electrode was removed from solution and subsequently rinsed with H_2O and dried under a stream of $N_{2(g)}$. The Au-coated substrate with top-facing photoelectrodeposit was mechanically separated from the rest of the electrode assembly. The nitrocellulose-based insulation and the majority of the Ag paint and In-Ga eutectic were then removed mechanically.

7.7 Film Analysis

SEMs were obtained with a FEI Nova NanoSEM 450 at an accelerating voltage of 5.00 kV with a working distance of 5 mm and an in-lens secondary electron detector. Micrographs obtained for quantitative analysis were acquired with a resolution of 172 pixels μm^{-1} over ~

120 μm^2 areas. Micrographs that were used to produce display figures were acquired with a resolution of 344 pixels μm^{-1} over ~ 2 μm^2 areas.

AFMs were collected with a Dimension Icon Atomic Force Microscope (Bruker Nano Surfaces) using ScanAsyst-Air probes (Bruker AFM Probes). Micrographs were collected with a resolution of 342 pixels μm^{-1} over ~ 1 μm^2 areas.

EDX spectroscopy was performed in the SEM using an accelerating voltage of 15.00 kV with a working distance of 5 mm. An Oxford Instruments X-Max Si drift detector was utilized. Spectra were collected in the range of 0 to 10 keV and quantitative film compositions were derived from these spectra using the "INCA" software package (Oxford Instruments).

GIXRD was performed using a Bruker D8 Discover diffractometer with a Cu Kα source and a two-dimensional Vantec detector. The X-rays were directed at a grazing angle $\omega = 0.3°$ above the plane of the sample surface and the detector was swept throughout the entire 2θ range.

7.8 Simulation of Film Growth

The growths of the photoelectrochemically deposited films were simulated with an iterative growth model in which electromagnetic simulations were first used to calculate the local photocarrier-generation rates at the film surface. Then, mass addition was simulated via a Monte Carlo method wherein the local photocarrier-generation rate weighted the local rate of mass addition along the film surface.

Growth simulations began with a bare, semi-infinite planar substrate. In the first step, the light-absorption profile under a linearly polarized, plane-wave illumination source was calculated using full-wave finite-difference time-domain (FDTD) simulations ("FDTD Solutions" software package, Lumerical) with periodic boundary conditions along the substrate interface. In the second step, a Monte Carlo simulation was performed in which an amount of mass, equaling that of a 15 nm (for the simulations presented in Chapter 2, Chapter 3, and Chapter 6) or 5 nm (for the simulations presented in Chapter 4 and Chapter 5) planar layer covering the simulation area, was added to the upper surface of the structure with a probability F:

$$F(G) = G\prod_{i=1}^{3}\frac{x_i}{r_i} \quad \textbf{(Equation 1)},$$

where G is the spatially dependent photocarrier-generation rate at the deposit/solution interface, x_i is the fraction of i^{th} nearest neighbors occupied in the cubic lattice, and r_i is the distance to the i^{th} nearest neighbor. The multiplicative sum in the definition of this probability (Equation 1) serves to reduce the surface roughness of the film so as to mimic the experimentally observed surface roughness. After the initial Monte Carlo simulation, the absorbance of the new, structured film was then calculated in the same manner as for the initial planar film, and an additional Monte Carlo simulation of mass addition was performed. For the simulations presented in Chapter 2 and Chapter 3, this process was repeated for a total of 18 iterations. For the simulations presented in Chapter 4 and Chapter 5, this process was repeated until the simulated morphologies achieved heights equivalent to those exhibited by the experimentally generated deposits. For the three-dimensional simulations presented in Chapter 6, this process was repeated for a total of 30 iterations. For the two-dimensional simulations presented in Chapter 6, this process was repeated until the simulated morphologies achieved height equivalent to those exhibited by the experimentally generated deposits. To model growth using two sequential, discrete illumination inputs, the computational process was also first iterated using the initial illumination input until the simulated morphology heights were equivalent to those exhibited by the experimentally generated deposits using that initial input. Then, the simulated illumination was updated to represent the new optical input, and the computational process was further iterated until the simulated morphologies achieved heights equivalent to those exhibited by the experimentally generated deposits for growth with sequential, discrete illumination inputs.

A value of n = 1.33 was used as the refractive index of the electrolyte, regardless of wavelength.[138] Previously measured values of the wavelength-dependent complex refractive index of Se-Te were utilized.[48] Simulations were performed using illumination inputs with λ_{avg} values and intensities matching those used experimentally (see Section 7.4). The E-field vector of the illumination was oriented parallel to the substrate. A cubic mesh with a lattice constant of 10 nm and 7 nm was used for discretization for the simulations presented in Chapter 2 and Chapter 3, respectively. A square mesh with a lattice constant of 5 nm was used for the simulations presented in Chapter 4 and Chapter 5 and for the two-dimensional simulations presented in Chapter 6. For the three-dimensional simulations presented in Chapter 6, a cubic mesh with a lattice constant of 7 nm was used for simulations with λ_{avg} = 366 nm and λ_{avg} = 454 nm; a cubic mesh with a lattice constant of 10 nm was used for simulation with λ_{avg} = 501 nm.

7.9 Simulation of Field Amplitude for Dipole Emitters

The time-averaged E-field amplitude resulting from two coherent dipole sources was calculated using two-dimensional FDTD simulations (“FDTD Solutions” software package, Lumerical). A square simulation plane was utilized. Dipoles were arranged with a separation of twice the emission wavelength and the oscillation axis was set perpendicular to the separation axis.

7.10 Simulation of Field Amplitude for Idealized Structures

Two-dimensional FDTD simulations (“FDTD Solutions” software package, Lumerical) were used to calculate the time-averaged E-field magnitude for illumination of idealized photoelectrodeposited structures. Structures were designed with dimensions derived from experimental data. The E-field vector of the illumination was oriented parallel to the substrate. A square simulation mesh was used with a lattice constant of 2 nm. Perfectly matched layer boundary conditions were imposed in the direction parallel to the propagation direction whereas periodic boundary conditions were imposed in the perpendicular direction.

BIBLIOGRAPHY

(1) Vukusic, P.; Sambles, J. R. Photonic Structures in Biology. *Nature* **2003**, *424* (6950), 852–855.

(2) Lawrence, C.; Vukusic, P.; Sambles, R. Grazing-Incidence Iridescence from a Butterfly Wing. *Appl. Opt., AO* **2002**, *41* (3), 437–441.

(3) Stavenga, D. g; Foletti, S.; Palasantzas, G.; Arikawa, K. Light on the Moth-Eye Corneal Nipple Array of Butterflies. *Proceedings of the Royal Society B: Biological Sciences* **2006**, *273* (1587), 661–667.

(4) Burton, Z.; Bhushan, B. Surface Characterization and Adhesion and Friction Properties of Hydrophobic Leaf Surfaces. *Ultramicroscopy* **2006**, *106* (8), 709–719.

(5) Neinhuis, C.; Barthlott, W. Characterization and Distribution of Water-Repellent, Self-Cleaning Plant Surfaces. *Ann Bot* **1997**, *79* (6), 667–677.

(6) Bargel, H.; Koch, K.; Cerman, Z.; Neinhuis, C.; Bargel, H.; Koch, K.; Cerman, Z.; Neinhuis, C. Structure–Function Relationships of the Plant Cuticle and Cuticular Waxes — a Smart Material? *Functional Plant Biol.* **2006**, *33* (10), 893–910.

(7) Matas, A. J.; Cobb, E. D.; Bartsch, J. A.; Paolillo Jr., D. J.; Niklas, K. J. Biomechanics and Anatomy of Lycopersicon Esculentum Fruit Peels and Enzyme-Treated Samples. *American Journal of Botany* **2004**, *91* (3), 352–360.

(8) Barthelat, F.; Yin, Z.; Buehler, M. J. Structure and Mechanics of Interfaces in Biological Materials. *Nat Rev Mater* **2016**, *1* (4), 1–16.

(9) Baker, K. M. Highly Corrected Close-Packed Microlens Arrays and Moth-Eye Structuring on Curved Surfaces. *Appl. Opt., AO* **1999**, *38* (2), 352–356.

(10) Kinoshita, S.; Yoshioka, S.; Fujii, Y.; Okamoto, N. Photophysics of Structural Color in the Morpho Butterflies. 19.

(11) Ding, Y.; Xu, S.; Wang, Z. L. Structural Colors from Morpho Peleides Butterfly Wing Scales. *Journal of Applied Physics* **2009**, *106* (7), 074702.

(12) Smith, G. S. Structural Color of Morpho Butterflies. *American Journal of Physics* **2009**, *77* (11), 1010–1019.

(13) Shevtsova, E.; Hansson, C.; Janzen, D. H.; Kjaerandsen, J. Stable Structural Color Patterns Displayed on Transparent Insect Wings. *Proceedings of the National Academy of Sciences* **2011**, *108* (2), 668–673.

(14) Anderson, T. F.; Richards, A. G. An Electron Microscope Study of Some Structural Colors of Insects. *Journal of Applied Physics* **1942**, *13* (12), 748–758.

(15) Simonis, P.; Vigneron, J. P. Structural Color Produced by a Three-Dimensional Photonic Polycrystal in the Scales of a Longhorn Beetle: Pseudomyagrus Waterhousei (Coleoptera: Cerambicidae). *Phys. Rev. E* **2011**, *83* (1), 011908.

(16) Welch, V. L.; Vigneron, J.-P. Beyond Butterflies—the Diversity of Biological Photonic Crystals. *Opt Quant Electron* **2007**, *39* (4), 295–303.

(17) Seago, A. E.; Brady, P.; Vigneron, J.-P.; Schultz, T. D. Gold Bugs and beyond: A Review of Iridescence and Structural Colour Mechanisms in Beetles (Coleoptera). *Journal of The Royal Society Interface* **2009**, *6* (suppl_2), S165–S184.

(18) C, F. D.; D, T. P.; M, D. R.; B, M. Y. Properties and Utilization of Shark Skin. *J. Entomol. Zool. Stud.* **2020**, *8* (1), 623–625.

(19) Ankhelyi, M. V.; Wainwright, D. K.; Lauder, G. V. Diversity of Dermal Denticle Structure in Sharks: Skin Surface Roughness and Three-Dimensional Morphology. *Journal of Morphology* **2018**, *279* (8), 1132–1154.

(20) Wang, J.; Chen, H.; Sui, T.; Li, A.; Chen, D. Investigation on Hydrophobicity of Lotus Leaf: Experiment and Theory. *Plant Science* **2009**, *176* (5), 687–695.

(21) Yang, F.; Guo, Z. Characterization of Micro-Morphology and Wettability of Lotus Leaf, Waterlily Leaf and Biomimetic ZnO Surface. *Journal of Bionic Engineering* **2015**, *12* (1), 88–97.

(22) Wang, L. F.; Dai, Z. D. Effects of the Natural Microstructures on the Wettability of Leaf Surfaces. *Biosurface and Biotribology* **2016**, *2* (2), 70–74.

(23) Ju, J.; Bai, H.; Zheng, Y.; Zhao, T.; Fang, R.; Jiang, L. A Multi-Structural and Multi-Functional Integrated Fog Collection System in Cactus. *Nat Commun* **2012**, *3* (1), 1247.

(24) Agrawal, A. A. Phenotypic Plasticity in the Interactions and Evolution of Species. *Science* **2001**, *294* (5541), 321–326.

(25) Satbhai, S. B.; Ristova, D.; Busch, W. Underground Tuning: Quantitative Regulation of Root Growth. *Journal of Experimental Botany* **2015**, *66* (4), 1099–1112.

(26) Hutchings, M. J.; de Kroon, H. Foraging in Plants: The Role of Morphological Plasticity in Resource Acquisition. In *Advances in Ecological Research*; Begon, M., Fitter, A. H., Eds.; Academic Press, 1994; Vol. 25, pp 159–238.

(27) Mou, P.; Jones, R. H.; Tan, Z.; Bao, Z.; Chen, H. Morphological and Physiological Plasticity of Plant Roots When Nutrients Are Both Spatially and Temporally Heterogeneous. *Plant and Soil* **2013**, *364* (1/2), 373–384.

(28) Blom, C. W. P. M.; Voesenek, L. A. C. J. Flooding: The Survival Strategies of Plants. *Trends in Ecology & Evolution* **1996**, *11* (7), 290–295.

(29) de Wit, M.; Pierik, R. Photomorphogenesis and Photoreceptors. In *Canopy Photosynthesis: From Basics to Applications*; Hikosaka, K., Niinemets, Ü., Anten, N. P. R., Eds.; Springer Netherlands: Dordrecht, 2016; pp 171–186.

(30) Arens, N. C.; Baracaldo, P. S. Variation in Tree Fern Stipe Length with Canopy Height: Tracking Preferred Habitat through Morphological Change. *Am. Fern. J.* **2000**, *90* (1), 1–15.

(31) Park, Y.; Runkle, E. S. Far-Red Radiation Promotes Growth of Seedlings by Increasing Leaf Expansion and Whole-Plant Net Assimilation. *Environmental and Experimental Botany* **2017**, *136*, 41–49.

(32) Fankhauser, C.; Chory, J. Light Control of Plant Development. *Annual Review of Cell and Developmental Biology* **1997**, *13* (1), 203–229.

(33) Christie, J. M.; Murphy, A. S. Shoot Phototropism in Higher Plants: New Light through Old Concepts. *Am J Bot* **2013**, *100* (1), 35–46.

(34) Tomlinson, P. B.; Tomlinson, P. B. *The Structural Biology of Palms*; Oxford science publications; Clarendon Press, 1990.

(35) Iwase, A.; Sakai, K.; Suzuki, A.; van Woesik, R. Phototropic Adjustment of the Foliaceous Coral Echinopora Lamellosa in Palau. *Estuarine, Coastal and Shelf Science* **2008**, *77* (4), 672–678.

(36) Ballare, C. L.; Scopel, A. L.; Roush, M. L.; Radosevich, S. R. How Plants Find Light in Patchy Canopies. A Comparison between Wild-Type and Phytochrome-B-Deficient Mutant Plants of Cucumber. *Functional Ecology* **1995**, *9* (6), 859–868.

(37) Huang, J.; Wang, X.; Wang, Z. L. Controlled Replication of Butterfly Wings for Achieving Tunable Photonic Properties. *Nano Lett.* **2006**, *6* (10), 2325–2331.

(38) Ko, D.-H.; R. Tumbleston, J.; J. Henderson, K.; E. Euliss, L.; M. DeSimone, J.; Lopez, R.; T. Samulski, E. Biomimetic Microlens Array with Antireflective "Moth-Eye" Surface. *Soft Matter* **2011**, *7* (14), 6404–6407.

(39) Serrà, A.; Zhang, Y.; Sepúlveda, B.; Gómez, E.; Nogués, J.; Michler, J.; Philippe, L. Highly Active ZnO-Based Biomimetic Fern-like Microleaves for Photocatalytic Water Decontamination Using Sunlight. *Applied Catalysis B: Environmental* **2019**, *248*, 129–146.

(40) Park, K.-C.; Choi, H. J.; Chang, C.-H.; Cohen, R. E.; McKinley, G. H.; Barbastathis, G. Nanotextured Silica Surfaces with Robust Superhydrophobicity and Omnidirectional Broadband Supertransmissivity. *ACS Nano* **2012**, *6* (5), 3789–3799.

(41) Shah, G. J.; Sitti, M. Modeling and Design of Biomimetic Adhesives Inspired by Gecko Foot-Hairs. In *2004 IEEE International Conference on Robotics and Biomimetics*; 2004; pp 873–878.

(42) Sun, T.; Feng, L.; Gao, X.; Jiang, L. Bioinspired Surfaces with Special Wettability. *Acc. Chem. Res.* **2005**, *38* (8), 644–652.

(43) Liu, K.; Du, J.; Wu, J.; Jiang, L. Superhydrophobic Gecko Feet with High Adhesive Forces towards Water and Their Bio-Inspired Materials. *Nanoscale* **2012**, *4* (3), 768–772.

(44) Lee, S. G.; Lim, H. S.; Lee, D. Y.; Kwak, D.; Cho, K. Tunable Anisotropic Wettability of Rice Leaf-Like Wavy Surfaces. *Advanced Functional Materials* **2013**, *23* (5), 547–553.

(45) Shang, L.; Yu, Y.; Gao, W.; Wang, Y.; Qu, L.; Zhao, Z.; Chai, R.; Zhao, Y. Bio-Inspired Anisotropic Wettability Surfaces from Dynamic Ferrofluid Assembled Templates. *Advanced Functional Materials* **2018**, *28* (7), 1705802.

(46) Guo, M.; Wang, Y.; Gao, B.; He, B. Shark Tooth-Inspired Microneedle Dressing for Intelligent Wound Management. *ACS Nano* **2021**, *15* (9), 15316–15327.

(47) Bhushan, B.; Jung, Y. C. Natural and Biomimetic Artificial Surfaces for Superhydrophobicity, Self-Cleaning, Low Adhesion, and Drag Reduction. *Progress in Materials Science* **2011**, *56* (1), 1–108.

(48) Sadtler, B.; Burgos, S. P.; Batara, N. A.; Beardslee, J. A.; Atwater, H. A.; Lewis, N. S. Phototropic Growth Control of Nanoscale Pattern Formation in Photoelectrodeposited Se-Te Films. *Proc. Natl. Acad. Sci. U. S. A.* **2013**, *110* (49), 19707–19712.

(49) Meier, M. C.; Cheng, W.-H.; Atwater, H. A.; Lewis, N. S.; Carim, A. I. Inorganic Phototropism in Electrodeposition of Se–Te. *J. Am. Chem. Soc.* **2019**, *141* (47), 18658–18661.

(50) Carim, A. I.; Batara, N. A.; Premkumar, A.; Atwater, H. A.; Lewis, N. S. Self-Optimizing Photoelectrochemical Growth of Nanopatterned Se–Te Films in

Response to the Spectral Distribution of Incident Illumination. *Nano Lett.* **2015**, *15* (10), 7071–7076.

(51) Carim, A. I.; Batara, N. A.; Premkumar, A.; May, R.; Atwater, H. A.; Lewis, N. S. Morphological Expression of the Coherence and Relative Phase of Optical Inputs to the Photoelectrodeposition of Nanopatterned Se–Te Films. *Nano Lett.* **2016**, *16* (5), 2963–2968.

(52) Carim, A. I.; Batara, N. A.; Premkumar, A.; Atwater, H. A.; Lewis, N. S. Polarization Control of Morphological Pattern Orientation During Light-Mediated Synthesis of Nanostructured Se–Te Films. *ACS Nano* **2016**, *10* (1), 102–111.

(53) Carim, A. I.; Meier, M. C.; Kennedy, K. M.; Richter, M. H.; Hamann, K. R.; Lewis, N. S. Assessing Effects of Near-Field Synergistic Light Absorption on Ordered Inorganic Phototropic Growth. *J. Am. Chem. Soc.* **2021**, *143* (10), 3693–3696.

(54) Simonoff, E.; Muñoz, L. X. V.; Lewis, N. S. Increased Spatial Randomness and Disorder of Nucleates in Dark-Phase Electrodeposition Lead to Increased Spatial Order and Pattern Fidelity in Phototropically Grown Se–Te Electrodeposits. *Nanoscale* **2020**, *12* (44), 22478–22486.

(55) Simonoff, E.; Lichterman, M. F.; Papadantonakis, K. M.; Lewis, N. S. Influence of Substrates on the Long-Range Order of Photoelectrodeposited Se–Te Nanostructures. *Nano Lett.* **2019**, *19* (2), 1295–1300.

(56) S.M.Sze; Ng, K. K. *Physics of Semiconductor Devices, 3rd Edition*; Wiley India Pvt. Limited, 2008.

(57) Bard, A. J.; Faulkner, L. R. *Electrochemical Methods: Fundamentals and Applications*; Wiley, 2000.

(58) Tan, M. X.; Laibinis, P. E.; Nguyen, S. T.; Kesselman, J. M.; Stanton, C. E.; Lewis, N. S. Principles and Applications of Semiconductor Photoelectrochemistry. In *Progress in Inorganic Chemistry*; John Wiley & Sons, Ltd, 1994; pp 21–144.

(59) Gamburg, Y. D.; Zangari, G. *Theory and Practice of Metal Electrodeposition*; SpringerLink : Bücher; Springer New York, 2011.

(60) Li, C.; Iqbal, M.; Lin, J.; Luo, X.; Jiang, B.; Malgras, V.; Wu, K. C.-W.; Kim, J.; Yamauchi, Y. Electrochemical Deposition: An Advanced Approach for Templated Synthesis of Nanoporous Metal Architectures. *Acc. Chem. Res.* **2018**, *51* (8), 1764–1773.

(61) Zheng, J.; Zhao, Q.; Tang, T.; Yin, J.; Quilty, C. D.; Renderos, G. D.; Liu, X.; Deng, Y.; Wang, L.; Bock, D. C.; Jaye, C.; Zhang, D.; Takeuchi, E. S.; Takeuchi, K. J.; Marschilok, A. C.; Archer, L. A. Reversible Epitaxial Electrodeposition of Metals in Battery Anodes. *Science* **2019**, *366* (6465), 645–648.

(62) Merrill, M. D.; Dougherty, R. C. Metal Oxide Catalysts for the Evolution of O2 from H2O. *J. Phys. Chem. C* **2008**, *112* (10), 3655–3666.

(63) Carim, A. I.; Saadi, F. H.; Soriaga, M. P.; Lewis, N. S. Electrocatalysis of the Hydrogen-Evolution Reaction by Electrodeposited Amorphous Cobalt Selenide Films. *J. Mater. Chem. A* **2014**, *2* (34), 13835–13839.

(64) Kempler, P. A.; Fu, H. J.; Ifkovits, Z. P.; Papadantonakis, K. M.; Lewis, N. S. Spontaneous Formation of >90% Optically Transmissive, Electrochemically Active CoP Films for Photoelectrochemical Hydrogen Evolution. *J. Phys. Chem. Lett.* **2020**, *11* (1), 14–20.

(65) Chauhan, S.; Rajaram, P. Electrodeposition of HgCdTe Thin Films. *Solar Energy Materials and Solar Cells* **2008**, *92* (5), 550–557.

(66) Fulop, G. F.; Taylor, R. M. Electrodeposition of Semiconductors. *Annual Review of Materials Science* **1985**, *15* (1), 197–210.

(67) Bhattacharya, R. N.; Hiltner, J. F.; Batchelor, W.; Contreras, M. A.; Noufi, R. N.; Sites, J. R. 15.4% CuIn1−xGaxSe2-Based Photovoltaic Cells from Solution-Based Precursor Films. *Thin Solid Films* **2000**, *361–362*, 396–399.

(68) Saraby-Reintjes, A.; Peter, L. M.; Özsan, M. E.; Dennison, S.; Webster, S. On the Mechanism of the Cathodic Electrodeposition of Cadmium Telluride. *J. Electrochem. Soc.* **1993**, *140* (10), 2880.

(69) Lee, S.; Lee, H. Electrodeposition of Conducting Polymers on Copper in Nonaqueous Media by Corrosion Inhibition. *Journal of Electrochemical Science and Technology 3* (2), 85–89.

(70) Fukuhara, Y.; Kyuzo, M.; Tsutsumi, Y.; Nagai, A.; Chen, P.; Hanawa, T. The Effect of Different Component Ratios in Block Polymers and Processing Conditions on Electrodeposition Efficiency onto Titanium. *Applied Surface Science* **2015**, *355*, 784–791.

(71) Liu, C.; Wang, K.; Luo, S.; Tang, Y.; Chen, L. Direct Electrodeposition of Graphene Enabling the One-Step Synthesis of Graphene–Metal Nanocomposite Films. *Small* **2011**, *7* (9), 1203–1206.

(72) Noori, Y. J.; Thomas, S.; Ramadan, S.; Smith, D. E.; Greenacre, V. K.; Abdelazim, N.; Han, Y.; Beanland, R.; Hector, A. L.; Klein, N.; Reid, G.; Bartlett, P. N.; Kees de Groot, C. H. Large-Area Electrodeposition of Few-Layer MoS2 on Graphene for 2D Material Heterostructures. *ACS Appl. Mater. Interfaces* **2020**, *12* (44), 49786–49794.

(73) Zhitomirsky, I. Cathodic Electrodeposition of Ceramic and Organoceramic Materials. Fundamental Aspects. *Advances in Colloid and Interface Science* **2002**, *97* (1), 279–317.

(74) Rodriguez, C. A. D.; Tremiliosi-Filho, G. Electrochemical Deposition. In *Encyclopedia of Tribology*; Wang, Q. J., Chung, Y.-W., Eds.; Springer US: Boston, MA, 2013; pp 918–922.

(75) Dharmadasa, I. M.; Haigh, J. Strengths and Advantages of Electrodeposition as a Semiconductor Growth Technique for Applications in Macroelectronic Devices. *J. Electrochem. Soc.* **2005**, *153* (1), G47.

(76) Schwarzacher, W. Electrodeposition: A Technology for the Future. *Electrochem. Soc. Interface* **2006**, *15* (1), 32–33.

(77) Menke, E. J.; Thompson, M. A.; Xiang, C.; Yang, L. C.; Penner, R. M. Lithographically Patterned Nanowire Electrodeposition. *Nature Materials* **2006**, *5* (11), 914–919.

(78) Moffat, T. P.; Yang, H. Patterned Metal Electrodeposition Using an Alkanethiolate Mask. *J. Electrochem. Soc.* **1995**, *142* (11), L220.

(79) Halpern, A. R.; Corn, R. M. Lithographically Patterned Electrodeposition of Gold, Silver, and Nickel Nanoring Arrays with Widely Tunable Near-Infrared Plasmonic Resonances. *ACS Nano* **2013**, *7* (2), 1755–1762.

(80) Audesirk, H. A.; Warren, E. L.; Ku, J.; Lewis, N. S. Ordered Silicon Microwire Arrays Grown from Substrates Patterned Using Imprint Lithography and Electrodeposition. *ACS Appl. Mater. Interfaces* **2015**, *7* (3), 1396–1400.

(81) Inoue, T.; Fujishima, A.; Honda, K. Photoelectrochemical Imaging Processes Using Semiconductor Electrodes. *Chem. Lett.* **1978**, *7* (11), 1197–1200.

(82) Souche, Y.; Lévy, J. P.; Wagner, E.; Liénard, A.; Alvarez-Prado, L.; Collins, R. T. Photoelectrodeposition of Patterned Cobalt Films on Silicon Substrates. *Journal of Magnetism and Magnetic Materials* **2002**, *242–245*, 578–580.

(83) Lim, S. Y.; Kim, Y.-R.; Ha, K.; Lee, J.-K.; Lee, J. G.; Jang, W.; Lee, J.-Y.; Bae, J. H.; Chung, T. D. Light-Guided Electrodeposition of Non-Noble Catalyst Patterns for Photoelectrochemical Hydrogen Evolution. *Energy Environ. Sci.* **2015**, *8* (12), 3654–3662.

(84) Vogel, Y. B.; Gonçales, V. R.; Al-Obaidi, L.; Gooding, J. J.; Darwish, N.; Ciampi, S. Nanocrystal Inks: Photoelectrochemical Printing of Cu2O Nanocrystals on Silicon with 2D Control on Polyhedral Shapes. *Advanced Functional Materials* **2018**, *28* (51), 1804791.

(85) Seo, D.; Lim, S. Y.; Lee, J.; Yun, J.; Chung, T. D. Robust and High Spatial Resolution Light Addressable Electrochemistry Using Hematite (α-Fe2O3) Photoanodes. *ACS Appl. Mater. Interfaces* **2018**, *10* (39), 33662–33668.

(86) Vogel, Y. B.; Gonçales, V. R.; Gooding, J. J.; Ciampi, S. Electrochemical Microscopy Based on Spatial Light Modulators: A Projection System to Spatially Address Electrochemical Reactions at Semiconductors. *J. Electrochem. Soc.* **2017**, *165* (4), H3085.

(87) Vogel, Y. B.; Gooding, J. J.; Ciampi, S. Light-Addressable Electrochemistry at Semiconductor Electrodes: Redox Imaging, Mask-Free Lithography and Spatially Resolved Chemical and Biological Sensing. *Chem. Soc. Rev.* **2019**, *48* (14), 3723–3739.

(88) Dasog, M.; Carim, A. I.; Yalamanchili, S.; Atwater, H. A.; Lewis, N. S. Profiling Photoinduced Carrier Generation in Semiconductor Microwire Arrays via Photoelectrochemical Metal Deposition. *Nano Lett.* **2016**, *16* (8), 5015–5021.

(89) Kontoleta, E.; Askes, S. H. C.; Lai, L.-H.; Garnett, E. C. Localized Photodeposition of Catalysts Using Nanophotonic Resonances in Silicon Photocathodes. *Beilstein J. Nanotechnol.* **2018**, *9* (1), 2097–2105.

(90) Freyland, W.; Zell, C. A.; Abedin, S. Z. E.; Endres, F. Nanoscale Electrodeposition of Metals and Semiconductors from Ionic Liquids. *Electrochimica Acta* **2003**, *48* (20), 3053–3061.

(91) de Carvalho, M. F.; Barbano, E. P.; Carlos, I. A. Influence of Disodium Ethylenediaminetetraacetate on Zinc Electrodeposition Process and on the Morphology, Chemical Composition and Structure of the Electrodeposits. *Electrochimica Acta* **2013**, *109*, 798–808.

(92) Stoychev, D.; Tsvetanov, C. Behaviour of Poly(Ethylene Glycol) during Electrodeposition of Bright Copper Coatings in Sulfuric Acid Electrolytes. *J Appl Electrochem* **1996**, *26* (7), 741–749.

(93) Haiss, W.; Nichols, R. J.; Sass, J.-K. In Situ Monitoring of Intrinsic Stress Changes during Copper Electrodeposition on Au(111). *Surface Science* **1997**, *388* (1), 141–149.

(94) Gira, M. J.; Tkacz, K. P.; Hampton, J. R. Physical and Electrochemical Area Determination of Electrodeposited Ni, Co, and NiCo Thin Films. *Nano Convergence* **2016**, *3* (1), 6.

(95) Norkus, E.; Vaškelis, A.; Stalnioniene, I. Changes of the Cu Electrode Real Surface Area during the Process of Electroless Copper Plating. *J Solid State Electrochem* **2000**, *4* (6), 337–341.

(96) Windheim, J. von; Cocivera, M. Photoelectrochemical Deposition of Cadmium Telluride Using Tri-N-Butylphosphine Telluride. *J. Electrochem. Soc.* **1987**, *134* (2), 440.

(97) Murase, K.; Matsui, M.; Miyake, M.; Hirato, T.; Awakura, Y. Photoassisted Electrodeposition of CdTe Layer from Ammoniacal Basic Aqueous Solutions. *J. Electrochem. Soc.* **2002**, *150* (1), C44.

(98) Arai, K.; Hagiwara, S.; Murase, K.; Hirato, T.; Awakura, Y. Galvanic Contact Deposition of CdTe Layers Using Ammoniacal Basic Aqueous Solution. *J. Electrochem. Soc.* **2005**, *152* (4), C237.

(99) Kamada, K.; Higashikawa, K.; Inada, M.; Enomoto, N.; Hojo, J. Photoassisted Anodic Electrodeposition of Ceria Thin Films. *J. Phys. Chem. C* **2007**, *111* (39), 14508–14513.

(100) Simonoff, E.; Thompson, J. R.; Meier, M. C.; Kennedy, K. M.; Hamann, K. R.; Lewis, N. S. Preseeded Optical Scatterers as a Template for Enhancing Order in Inorganic Phototropic Growth. *J. Phys. Chem. C* **2021**, *125* (17), 9571–9581.

(101) Carim, A. I.; Hamann, K. R.; Batara, N. A.; Thompson, J. R.; Atwater, H. A.; Lewis, N. S. Template-Free Synthesis of Periodic Three-Dimensional PbSe Nanostructures via Photoelectrodeposition. *J. Am. Chem. Soc.* **2018**, *140* (21), 6536–6539.

(102) Hamann, K. R.; Carim, A. I.; Meier, M. C.; Thompson, J. R.; Batara, N. A.; Yermolenko, I. S.; Atwater, H. A.; Lewis, N. S. Optically Tunable Mesoscale CdSe Morphologies via Inorganic Phototropic Growth. *J. Mater. Chem. C* **2020**, *8* (36), 12412–12417.

(103) Hamann, K. R.; Meier, M. C.; Lewis, N. S.; Carim, A. I. Plastic Morphological Response to Spectral Shifts during Inorganic Phototropic Growth. *JACS Au* **2022**, *2* (4), 865–874.

(104) Hamann, K. R.; Carim, A. I.; Meier, M. C.; Lewis, N. S. Path-Dependent Morphological Evolution of Se–Te Mesostructures Prepared by Inorganic Phototropic Growth. *J. Am. Chem. Soc.* **2020**, *142* (47), 19840–19843.

(105) Ellingson, R. J.; Beard, M. C.; Johnson, J. C.; Yu, P.; Micic, O. I.; Nozik, A. J.; Shabaev, A.; Efros, A. L. Highly Efficient Multiple Exciton Generation in Colloidal PbSe and PbS Quantum Dots. *Nano Lett.* **2005**, *5* (5), 865–871.

(106) Pijpers, J. J. H.; Ulbricht, R.; Tielrooij, K. J.; Osherov, A.; Golan, Y.; Delerue, C.; Allan, G.; Bonn, M. Assessment of Carrier-Multiplication Efficiency in Bulk PbSe and PbS. *Nature Phys* **2009**, *5* (11), 811–814.

(107) Kirschner, M. S.; Diroll, B. T.; Brumberg, A.; Leonard, A. A.; Hannah, D. C.; Chen, L. X.; Schaller, R. D. Optical Signatures of Transiently Disordered Semiconductor Nanocrystals. *ACS Nano* **2018**, *12* (10), 10008–10015.

(108) Sargent, E. H. Infrared Photovoltaics Made by Solution Processing. *Nature Photon* **2009**, *3* (6), 325–331.

(109) Martin, J. M.; Hernández, J. L.; Adell, L.; Rodriguez, A.; López, F. Arrays of Thermally Evaporated PbSe Infrared Photodetectors Deposited on Si Substrates Operating at Room Temperature. *Semicond. Sci. Technol.* **1996**, *11* (11), 1740–1744.

(110) Sukhovatkin, V.; Hinds, S.; Brzozowski, L.; Sargent, E. H. Colloidal Quantum-Dot Photodetectors Exploiting Multiexciton Generation. *Science* **2009**, *324* (5934), 1542–1544.

(111) Wang, H.; Pei, Y.; LaLonde, A. D.; Snyder, G. J. Heavily Doped P-Type PbSe with High Thermoelectric Performance: An Alternative for PbTe. *Advanced Materials* **2011**, *23* (11), 1366–1370.

(112) Lister, T. E.; Stickney, J. L. Atomic Level Studies of Selenium Electrodeposition on Gold(111) and Gold(110). *J. Phys. Chem.* **1996**, *100* (50), 19568–19576.

(113) Colletti, L. P.; Flowers, B. H.; Stickney, J. L. Formation of Thin Films of CdTe, CdSe, and CdS by Electrochemical Atomic Layer Epitaxy. *J. Electrochem. Soc.* **1998**, *145* (5), 1442.

(114) Peng, X.; Manna, L.; Yang, W.; Wickham, J.; Scher, E.; Kadavanich, A.; Alivisatos, A. P. Shape Control of CdSe Nanocrystals. *Nature* **2000**, *404* (6773), 59–61.

(115) Murray, C. B.; Kagan, C. R.; Bawendi, M. G. Synthesis and Characterization of Monodisperse Nanocrystals and Close-Packed Nanocrystal Assemblies. *Annual Review of Materials Science* **2000**, *30* (1), 545–610.

(116) Yin, Y.; Alivisatos, A. P. Colloidal Nanocrystal Synthesis and the Organic–Inorganic Interface. *Nature* **2005**, *437* (7059), 664–670.

(117) Storhoff, J. J.; Mucic, R. C.; Mirkin, C. A. Strategies for Organizing Nanoparticles into Aggregate Structures and Functional Materials. *Journal of Cluster Science* **1997**, *8* (2), 179–216.

(118) Vlasov, Y. A.; Yao, N.; Norris, D. J. Synthesis of Photonic Crystals for Optical Wavelengths from Semiconductor Quantum Dots. *Advanced Materials* **1999**, *11* (2), 165–169.

(119) Lin, Y.; Böker, A.; He, J.; Sill, K.; Xiang, H.; Abetz, C.; Li, X.; Wang, J.; Emrick, T.; Long, S.; Wang, Q.; Balazs, A.; Russell, T. P. Self-Directed Self-Assembly of Nanoparticle/Copolymer Mixtures. *Nature* **2005**, *434* (7029), 55–59.

(120) Xu, D.; Shi, X.; Guo, G.; Gui, L.; Tang, Y. Electrochemical Preparation of CdSe Nanowire Arrays. *J. Phys. Chem. B* **2000**, *104* (21), 5061–5063.

(121) Schierhorn, M.; Boettcher, S. W.; Kraemer, S.; Stucky, G. D.; Moskovits, M. Photoelectrochemical Performance of CdSe Nanorod Arrays Grown on a Transparent Conducting Substrate. *Nano Lett.* **2009**, *9* (9), 3262–3267.

(122) Lee, J.-S.; Kovalenko, M. V.; Huang, J.; Chung, D. S.; Talapin, D. V. Band-like Transport, High Electron Mobility and High Photoconductivity in All-Inorganic Nanocrystal Arrays. *Nature Nanotech* **2011**, *6* (6), 348–352.

(123) Penner, R. M. Electrodeposited Nanophotonics. *J. Phys. Chem. C* **2014**, *118* (31), 17179–17192.

(124) Huynh, W. U.; Dittmer, J. J.; Alivisatos, A. P. Hybrid Nanorod-Polymer Solar Cells. *Science* **2002**, *295* (5564), 2425–2427.

(125) Tomkiewicz, M.; Ling, I.; Parsons, W. S. Morphology, Properties, and Performance of Electrodeposited n - CdSe in Liquid Junction Solar Cells. *J. Electrochem. Soc.* **1982**, *129* (9), 2016.

(126) Colvin, V. L.; Schlamp, M. C.; Alivisatos, A. P. Light-Emitting Diodes Made from Cadmium Selenide Nanocrystals and a Semiconducting Polymer. *Nature* **1994**, *370* (6488), 354–357.

(127) Xing, W.; Yan, W.; Ayvazian, T.; Wang, Y.; Potma, E. O.; Penner, R. M. Electrodeposited Light-Emitting Nanojunctions. *Chem. Mater.* **2013**, *25* (4), 623–631.

(128) Kinoshita, S.; Yoshioka, S. Structural Colors in Nature: The Role of Regularity and Irregularity in the Structure. *ChemPhysChem* **2005**, *6* (8), 1442–1459.

(129) Saunders, A. P. The Allotropic Forms of Selenium. *J. Phys. Chem.* **1900**, *4* (6), 423–513.

(130) Moody, J. W.; Himes, R. C. Monoclinic Selenium Crystal Growth. *Materials Research Bulletin* **1967**, *2* (7), 523–530.

(131) Vukusic, P.; Sambles, J. R.; Lawrence, C. R. Colour Mixing in Wing Scales of a Butterfly. *Nature* **2000**, *404* (6777), 457–457.

(132) Zheng, Y.; Gao, X.; Jiang, L. Directional Adhesion of Superhydrophobic Butterfly Wings. *Soft Matter* **2007**, *3* (2), 178–182.

(133) Slade, A. J.; Hutchings, M. J. The Effects of Light Intensity on Foraging in the Clonal Herb Glechoma Hederacea. *Journal of Ecology* **1987**, *75* (3), 639–650.

(134) Schwinning, S.; Weiner, J. Mechanisms Determining the Degree of Size Asymmetry in Competition among Plants. *Oecologia* **1998**, *113* (4), 447–455.

(135) Farrior, C. E.; Bohlman, S. A.; Hubbell, S.; Pacala, S. W. Dominance of the Suppressed: Power-Law Size Structure in Tropical Forests. *Science* **2016**, *351* (6269), 155–157.

(136) Finlayson, S. A.; Krishnareddy, S. R.; Kebrom, T. H.; Casal, J. J. Phytochrome Regulation of Branching in Arabidopsis. *Plant Physiology* **2010**, *152* (4), 1914–1927.

(137) Chen, Z.; Cummins, D.; Reinecke, B. N.; Clark, E.; Sunkara, M. K.; Jaramillo, T. F. Core–Shell MoO3–MoS2 Nanowires for Hydrogen Evolution: A Functional Design for Electrocatalytic Materials. *Nano Lett.* **2011**, *11* (10), 4168–4175.

(138) Hale, G. M.; Querry, M. R. Optical Constants of Water in the 200-Nm to 200-Mm Wavelength Region. *Appl. Opt.* **1973**, *12* (3), 555–563.